# Asymptotic-preserving semi-implicit finite volume scheme for Extended Magnetohydrodynamics

Yi Han Toh, Joshua Dolence, Karthik Duraisamy University of Michigan & Los Alamos National Laboratory,

# Abstract

A Finite Volume (FV) scheme is developed for solving the extended magnetohydrodynamic (XMHD) equations, yielding accurate results in the ideal, resistive, and Hall MHD limits. This is accomplished by first re-writing the XMHD equations such that it allows the algorithm to retain the use of ideal MHD Riemann solvers and the constrained transport method to preserve divergence-free magnetic fields. Incorporation of electron inertia and displacement current introduces additional numerical stiffness which motivates a semi-implicit FV scheme that re-formulates the XMHD model as a relaxation system. The equations are then advanced in time using an explicit 2nd-order Runge-Kutta scheme with operator splitting applied to the implicit source term updates at each sub-stage. For additional numerical stability, density-dependent slope limiter is implemented to increase flux diffusivity at low density where non-ideal effects become significant. The algorithm is subsequently implemented on Artemis, a multifluid radiation hydrodynamics code built on Parthenon framework for high-performance computing (HPC) and adaptive mesh refinement (AMR) support. As the new algorithm retains many aspects of the ideal MHD formulations, it asymptotes naturally to the ideal MHD limit. Moreover, it shows promising results at the resistive and Hall MHD limits. This is verified against published test problems for ideal, resistive and Hall MHD.

 $\it Keywords: \, Extended \, Magnetohydrodynamics, Field diffusion, Hall drift waves, Resistive \, MHD$ 

## 1. Introduction

In high-energy-density (HED) plasma systems such as magnetized liner inertial fusion (MagLIF) implosions, inertial confinement fusion (ICF) experiments [1], Z-pinch implosions [2], X-pinches [3], tokamak disruptions [4] and pulsed-power systems [5], one must model plasmas that span a wide dynamic range of current-carrying densities. At sufficiently low densities, where the characteristic scale lengths become comparable to the ion inertial length, the single-fluid description provided by ideal magnetohydrodynamics (MHD) breaks down. This occurs because ideal MHD, despite its broad applicability, is valid only in certain regimes that satisfy certain simplifying assumptions [6]. Ideal MHD is typically derived as a limiting case of the two-fluid model which is obtained from the moments of the Boltzmann equation [6, 7]. When the two-fluid equations are reformulated in terms of one-fluid variables

(the center-of-mass velocity and the current density) together with some other concomitant simplifications, the resulting framework is known as Extended MHD (XMHD) [6].

XMHD incorporates two key two-fluid effects necessary for HED plasma systems: (i) the Hall drift arising from the difference between ion and electron fluid velocities and (ii) electron inertia which reflects the finite but small electron mass. Neglecting these two effects recovers the ideal MHD limit, whereas assuming massless electrons leads to the Hall MHD model. Although the concept of XMHD has been recognized at least since the 1950s [8], it has largely been explored from a theoretical standpoint until recent years. As one approaches smaller spatial scales, extended MHD effects become increasingly significant. Specifically, the ideal MHD regime applies for  $L > \lambda_i$ , the Hall MHD regime applies for  $\lambda_i > L > \lambda_e$  while the electron-inertia-dominated regime for  $L < \lambda_e$ , where L is a characteristic scale length and  $\lambda_s = c/\omega_{ps}$  denotes the skin depth of species s. While extended MHD provides a more general description than ideal MHD, it remains a fluid model and thus does not capture kinetic phenomena such as Landau damping or dissipative effects such as viscosity and resistivity unless these are explicitly included.

Having established that two-fluid MHD model is preferable to the single-fluid MHD model for high-energy-density (HED) plasma systems, especially in low-density regimes where characteristic scale lengths approach the ion inertial length, the applicability of existing numerical methods [9, 10, 11, 12, 13, 14] in this regime however remains limited. Chacon and Knoll [9] develop a fully implicit Hall MHD scheme through the use of a Jacobian-Free Newton-Krylov (JFNK) method to overcome stiffness associated with dispersive waves, but the solver is incompressible. For compressible flow, Hakim et al. [11] solved the ten-moment two-fluid plasma model which evolves the full pressure tensor to capture Hall and finite Larmor radius (FLR) effects, enabling simulation of small-scale instabilities and magnetic reconnection beyond ideal MHD. However, the model ignores collisional relaxation, causing the solutions to deviate significantly from ideal MHD in models of magnetic shock tubes due to the production of dispersive waves arising from the source terms.

Another type of two-fluid plasma model involves coupling the electron and ion fluids with electromagnetic fields through an approximate Riemann solver and a locally implicit treatment of source terms to account for stiffness [14]. This allows for the representation of phenomena beyond standard MHD models like Hall effects and diamagnetic currents but it is unclear if the solver is able to preserve  $\nabla \cdot \mathbf{B} = 0$  since all variables, including the magnetic field, are co-located. An alternative approach that explicitly enforces a divergence-free magnetic field is the Naval Research Laboratory (NRL)'s 3D Hall MHD code VooDoo [12]. It employs a finite volume method on a staggered Yee grid, with the magnetic field  $\mathbf{B}$  defined on cell faces, the electric field  $\mathbf{E}$  along cell edges, and all other variables at the cell centers. The code uses a distribution function approach to compute mass, momentum, and energy fluxes as well as the convective electric field [15], combined with a partial donor-cell method for flux limiting. However, electron inertia effects were ignored and the Hall term is sub-cycled for efficiency. To address these issues, Zhao et al. [16] developed a positivity-preserving discontinuous Galerkin (DG) scheme that ensures both the preservation of positive physical quantities and a locally divergence-free magnetic field in XMHD systems, thereby

maintaining numerical stability.

In their approach, Zhao et al. employ a relaxation algorithm to solve the coupled generalized Ohm's law (GOL) and Maxwell–Ampere's law for the electric field. This relaxation method is a semi-implicit time discretization technique that converges to the solution of the algebraic equations obtained by setting the stiff source terms to zero. For the XMHD system, this implies convergence to the GOL when electron inertial terms are neglected, and to Ampere's law when the displacement current term is neglected. By using this relaxation approach, the algorithm overcomes constraints associated with under-resolved stiff source terms, allowing time steps to exceed electron plasma and cyclotron frequency scales, therefore enabling the XMHD equations to be integrated on MHD time scales. Moreover, the Hall term is treated locally and implicitly which avoids the computational cost of solving large linear systems.

An additional advantage of the XMHD formulation is that in low-density regions, the current is naturally suppressed by both Hall and electron inertia effects. This enables the use of the unmodified Spitzer resistivity, ensuring a smooth and physically consistent plasma-vacuum transition. This relaxation algorithm has also been implemented in an XMHD code using 2nd-order finite volume (FV) scheme named PERSEUS (Plasma as an Extended-MHD Relaxation System using an Efficient Upwind Scheme) [17]. Using this framework, Zhao et al. successfully simulated a low-density magnetic shock tube problem, demonstrating the robustness and applicability of their method. However, the results remain oscillatory both at low and high density (e.g., Brio Wu shocktube). This motivates the current work which is to develop an XMHD solver that is not only stable at low density but asymptotic-preserving at the high density limit where it will produce similar results to the already well-established ideal MHD results.

The remainder of this paper is organized as follows. Section 2 describes the governing equations of the XMHD model and a re-formulation into a new form that allows one to retain most of the ideal MHD framework as well as its non-dimensional form and associated relaxation parameters. Section 3 focuses on the numerical setup for solving the new form of XMHD equations, including discretization, interpolation and order of accuracy. Section 4 presents a range of test cases to test the accuracy of the XMHD solver at ideal vs resistive vs Hall MHD limits. Classical ideal MHD problems are also tested but at different densities to show the deviation from ideal MHD results due to the increment of non-ideal effects. Concluding remarks are then provided in the final section.

# 2. Governing equations

The quasi-neutral  $(n_e = Zn_i = nZ)$  extended magnetohydrodynamics (XMHD) model is described as [16]

$$\frac{\partial \rho}{\partial t} + \nabla \cdot (\rho \mathbf{u}) = 0 \tag{1}$$

$$\frac{\partial}{\partial t}(\rho \mathbf{u}) + \nabla \cdot (\rho \mathbf{u} \mathbf{u} + P \mathbb{I}) = \mathbf{J} \times \mathbf{B}$$
 (2)

$$\frac{\partial E_n}{\partial t} + \nabla \cdot [\mathbf{u}(E_n + P)] = \mathbf{u} \cdot (\mathbf{J} \times \mathbf{B}) + \eta J^2$$
(3)

$$\frac{\partial \mathbf{B}}{\partial t} + \nabla \times \mathbf{E} = 0 \tag{4}$$

$$\frac{\partial \mathbf{E}}{\partial t} - c^2 \nabla \times \mathbf{B} = -\frac{1}{\epsilon_0} \mathbf{J} \tag{5}$$

$$\frac{\partial \mathbf{J}}{\partial t} + \nabla \cdot \left[ \mathbf{u} \mathbf{J} + \mathbf{J} \mathbf{u} - \frac{1}{n_e e} \mathbf{J} \mathbf{J} - \frac{e}{m_e} P_e \mathbb{I} \right] = \frac{n_e e^2}{m_e} \left[ \mathbf{E} + \mathbf{u} \times \mathbf{B} - \eta \mathbf{J} - \frac{1}{n_e e} \mathbf{J} \times \mathbf{B} \right]$$
(6)

$$\frac{\partial S_e}{\partial t} + \nabla \cdot (\mathbf{u}_e S_e) = (\gamma - 1) n_e^{1 - \gamma} \eta J^2, \tag{7}$$

where  $\eta$  is resistivity,  $\rho = m_i n_i + m_e n_e$ ,  $\mathbf{J} = e(Z n_i \mathbf{u}_i - n_e \mathbf{u}_e)$ ,  $\mathbf{u}_e = \mathbf{u} - \frac{\mathbf{J}}{n_e e}$ ,  $\mathbf{Z}$  is net ion charge,  $P_e = S_e n_e^{\gamma-1}$  is electron pressure,  $E_n = \rho e + \frac{1}{2}\rho u^2$  is hydrodynamic energy density and assumed ideal equation of state thus,  $\rho e = \frac{P}{\gamma-1}$ . Including electron inertia allows for a consistent treatment of low-density or vacuum regions, eliminating the need to introduce an artificial vacuum resistivity. The complete electromagnetic formulation of Maxwell's equations, together with the Hall term, ensures a self-consistent calculation of all electric field components and allows one to properly apply general boundary conditions to the problem [17]. Moreover, including both electron inertia and displacement current ensures Whistler waves to resonate at the cyclotron frequency which prevents the wave velocity to grow unbounded with frequency, hence helping to stabilize the Hall term [14]. However, they introduced additional numerical stiffness which motivates a semi-implicit scheme that will be detailed below. As for the electron equation of state, it is modeled using the electron entropy density  $S_e = \frac{P_e}{n_e^{\gamma-1}}$  as it gives rise to a positive definite source term which guarantees that the electron pressure is positive for numerical stability [16]. The limitation is that one cannot capture weak solutions in the form of electron shocks like Langmuir shocks. But since the focus here is on low frequency phenomena, well below the electron plasma frequency, this use of electron entropy is reasonable in this context.

# 2.1. Reformulation of governing equations

In both the momentum (2) and energy (3) equations, the magnetic field contributions are treated as source terms. As a result, the Rankine–Hugoniot conditions are not fully captured by the flux formulation and must be corrected by the source term, which may still lead to inaccuracies near discontinuities like in Fig. 3 from Zhao et. al. [16]. Therefore,

Eqs. 1 to 4 must be re-written to preserve ideal MHD equations on the left-hand side while the additional physics associated with extended MHD will be placed at the right-hand side as source term. The new form of extended MHD based on above Eqs. 1 to 7 is then written as follows

$$\frac{\partial \rho}{\partial t} + \nabla \cdot (\rho \mathbf{u}) = 0 \tag{8}$$

$$\frac{\partial}{\partial t}(\rho \mathbf{u}) + \nabla \cdot \left[ \rho \mathbf{u} \mathbf{u} - \frac{1}{\mu_0} \mathbf{B} \mathbf{B} + \left( P + \frac{1}{2\mu_0} B^2 \right) \mathbb{I} \right] = \left( \mathbf{J} - \frac{1}{\mu_0} \nabla \times \mathbf{B} \right) \times \mathbf{B}$$
(9)

$$\frac{\partial}{\partial t} \left( E_n + \frac{1}{2\mu_0} B^2 \right) + \nabla \cdot \left[ \mathbf{u} \left( E_n + P + \frac{1}{\mu_0} B^2 \right) - \frac{1}{\mu_0} (\mathbf{B} \cdot \mathbf{u}) \mathbf{B} \right]$$
(10)

$$= -\frac{1}{\mu_0} \mathbf{B} \cdot \left[ \nabla \times (\mathbf{E} + \mathbf{u} \times \mathbf{B}) \right] + \mathbf{u} \cdot \left( \left( \mathbf{J} - \frac{1}{\mu_0} \nabla \times \mathbf{B} \right) \times \mathbf{B} \right) + \eta J^2$$

$$\frac{\partial \mathbf{B}}{\partial t} - \nabla \cdot (\mathbf{B}\mathbf{u} - \mathbf{u}\mathbf{B}) = -\nabla \times (\mathbf{E} + \mathbf{u} \times \mathbf{B})$$
 (11)

$$\frac{\partial \mathbf{E}}{\partial t} - c^2 \nabla \times \mathbf{B} = -\frac{1}{\epsilon_0} \mathbf{J} \qquad (12)$$

$$\frac{\partial \mathbf{J}}{\partial t} + \nabla \cdot \left[ \mathbf{u} \mathbf{J} + \mathbf{J} \mathbf{u} - \frac{1}{n_e e} \mathbf{J} \mathbf{J} - \frac{e}{m_e} P_e \mathbb{I} \right] = \frac{n_e e^2}{m_e} \left[ \mathbf{E} + \mathbf{u} \times \mathbf{B} - \eta \mathbf{J} - \frac{1}{n_e e} \mathbf{J} \times \mathbf{B} \right]$$
(13)

$$\frac{\partial S_e}{\partial t} + \nabla \cdot (\mathbf{u}_e S_e) = (\gamma - 1) n_e^{1 - \gamma} \eta J^2. \tag{14}$$

The above derivation can be found in Appendix A.

For ideal MHD, plasma density is high which means that a large  $n_e$  will render the left-hand side (electron inertia and pressure term) and the Hall-term on the right-hand side of Eq. 13 to negligible as compared to the specific form of resistive Ohm's law. Additionally, ideal MHD assumed infinite conductivity and thus, Eq. 13 reduced to  $\mathbf{E} = -\mathbf{u} \times \mathbf{B}$ . This will subsequently reduce Eq. 11 to that of ideal MHD's induction equation. Additionally, ideal MHD assumes a non-relativistic regime, which means that the Ampere's law in Eq. 12 (or  $\frac{1}{c^2} \frac{\partial \mathbf{E}}{\partial t} - \nabla \times \mathbf{B} = -\mu_0 \mathbf{J}$ ) will simplify to  $\mathbf{J} = \frac{1}{\mu_0} \nabla \times \mathbf{B}$ . This will then eliminate the source term of Eq. 9, recovering the ideal MHD's momentum equation. The above reductions make the right-hand side of Eq. 10 go to zero, simplifying it to the ideal MHD energy equation. Most importantly, the jump conditions across the shocks will be preserved at the ideal MHD limit and this also allows the user to use existing MHD Riemann solvers like LLF or HLLD to solve for the left-hand side of Eqs. 8 to 11.

Eqs. 12 and 13 can then be non-dimensionalized (details in Appendix B) to obtain the non-dimensional parameters which characterize relaxation [16] as follows,

$$\frac{\partial \mathbf{E}}{\partial t} = \frac{c^2}{v^2} (\nabla \times \mathbf{B} - \mathbf{J}) \tag{15}$$

$$\frac{\partial \mathbf{J}}{\partial t} + \nabla \cdot \left[ \mathbf{u} \mathbf{J} + \mathbf{J} \mathbf{u} - \frac{\lambda_i}{L_0 n} \mathbf{J} \mathbf{J} - \frac{m_i L_0}{m_e \lambda_i} P_e \mathbb{I} \right] = \frac{L_0^2 n}{\lambda_e^2} \left[ \mathbf{E} + \mathbf{u} \times \mathbf{B} - \frac{\lambda_i}{L_0 n} \mathbf{J} \times \mathbf{B} - \eta \mathbf{J} \right], \quad (16)$$

where  $v = \frac{L_0}{t_0}$  is the characteristic speed while  $L_0$  and  $t_0$  are the representative length and time, respectively. The electron and ion inertial lengths are  $\lambda_j^2 = \frac{m_j}{n_0 e^2 \mu_0}$ . These give the relaxation parameters  $\frac{c^2}{v^2}$  and  $\frac{L_0^2 n}{\lambda_e^2}$  in above Eqs. 15 and 16, respectively. The remaining non-dimensionalized equations are

$$\frac{\partial \mathbf{B}}{\partial t} - \nabla \cdot (\mathbf{B}\mathbf{u} - \mathbf{u}\mathbf{B}) = -\nabla \times (\mathbf{E} + \mathbf{u} \times \mathbf{B})$$
 (20)

$$\frac{\partial S_e}{\partial t} + \nabla \cdot (\mathbf{u}_e S_e) = \frac{B_0^2}{\mu_0 n_0 m_i v^2} (\gamma - 1) n_e^{1-\gamma} \eta J^2, \quad (21)$$

where  $\frac{B_0^2}{\mu_0 n_0 m_i v^2}$  is the coefficient for the explicit source terms that arises from non-dimensionalization and the dimensional constants should be chosen such that  $\frac{B_0^2}{\mu_0 n_0 m_i v^2}$  is  $\sim 1$ . This does not necessary yield the best result which will be shown in one of the test case in Section 4.2 below but it serves as a good starting point to simplify the complexity of the above equations.

The phenomena of interest in high energy density (HED) plasmas happens at time scales much slower than the characteristic electron plasma and cyclotron frequencies, meaning that  $v \ll c$  and  $\lambda_e \ll L_0$ , respectively. This forces Eqs. 15 and 16 to relax to equilibrium as follows,

$$\nabla \times \mathbf{B} = \mathbf{J} \tag{22}$$

$$\mathbf{E} + \mathbf{u} \times \mathbf{B} - \frac{\lambda_i}{L_0 n} \mathbf{J} \times \mathbf{B} + \frac{\lambda_i}{L_0 n} \nabla P_e = \eta \mathbf{J}.$$
 (23)

Thus, when the electron inertial scale is under-resolved, the solution to Eqs. 15 and 16 will relax to the non-relativistic Ampere's law and inertia-less Generalized Ohm's law (GOL) in above Eqs. 22 and 23.

## 2.2. Strongly collisional plasma

One limitation of the above set of XMHD equations is that it does not contain source term to equilibrate ions and electrons temperature as the plasma becomes strongly collisional. To account for this, a more general equation for the electron entropy equation is considered

$$\frac{\partial S_e}{\partial t} + \nabla \cdot (\mathbf{u}_e S_e) = Q_{ei} \tag{24}$$

The quasineutrality assumption then allows the electron-ion interaction to be written as [18]

$$Q_{ei} = \nu_{ei}^g (T_i - T_e) + \zeta_{ei} \eta J^2 \tag{25}$$

The electron entropy equation can then be written as

$$\frac{\partial S_e}{\partial t} + \nabla \cdot (\mathbf{u}_e S_e) = n_e^{1-\gamma} (\gamma - 1) \left[ \nu_{ei}^g (T_i - T_e) + \xi_{ei} \eta J^2 \right]$$
 (26)

where the electron-ion exchange coefficient rate is  $\nu_{ei}^g = \frac{3}{2} k_B \frac{n_e n_i}{\tau_{ie} n_e + \tau_{ei} n_i}$  and take  $\nu_{ie} = \frac{n_e m_e}{n_i m_i} \nu_{ei}$  by assuming that both ions and electrons are close to thermal (Maxwellian) distributions where their momentum exhanges are symmetric. As seen from Eq. 7, Zhao et. al. [16] drops the  $\nu_{ei}^g$  term and takes  $\xi_{ei}$  as 1 by assuming that Ohmic heating between electrons and ions is similar. Therefore, some of the problem parameters used in the shocktube test case are chosen by Zhao et. al. such that the electron-ion energy exchange source term is weak. As a result, the exchange term is neglible over the simulation time, and  $T_i$  and  $T_e$  are not expected to equilibrate. We use the same parameter regime when testing the XMHD algorithm at the ideal MHD limit in this paper.

This is reasonable as in the ideal MHD limit, the macroscopic dynamics depend only on the total pressure (e.g.,  $P = P_i + P_e$ ) which enters the momentum (Eq. 18) and energy (Eq. 19) equations in exactly the same way as in the single-temperature ideal MHD system. This is assuming that Ampere's law and GOL relax to  $\mathbf{J} = \nabla \times \mathbf{B}$  and  $\mathbf{E} = -\mathbf{u} \times \mathbf{B}$  such that the non-ideal effects go to zero. Subsequently, the electron pressure effects do not have a leading order effect on the macroscopic dynamics (see Sect. 3.3 for more details) and hence, the partition of P into  $P_i$  and  $P_e$  becomes dynamically irrelevant in this limit.

Therefore, although the electron-ion energy exchange source term is small in the parameter regime used for the ideal MHD limit and does not equilibrate  $T_i$  and  $T_e$  over the simulated timescale, this has negligible impact on the ideal MHD evolution. This is because the equations reduced to the correct single-fluid ideal MHD form since only the total pressure controls the dynamics. In other regimes like the Hall MHD limit, the electron-ion energy exchange is naturally small due to low density involved. For brevity, the electron-ion energy exchange source term is then omitted from the electron entropy equation in the remainder of the paper. However, accurate modeling of  $T_i$  and  $T_e$  becomes crucial in regimes where radiation or other electron-specific physics are significant and this source term is demonstrated in Appendix C.

## 3. Numerical formulation

The MHD solver is implemented in Artemis, a multifluid radiation hydrodynamics code built on the Parthenon [19] high-performance computing (HPC) library, which includes adaptive mesh refinement (AMR) support. This is accomplished by first implementing ideal MHD in Artemis and verifying against common ideal MHD test problems from Athena++ [20] before extending the MHD solver to include additional physics such as resistivity and Hall effects from extended MHD based on Eqs. 8 to 14. However, several strategies should be

considered before discretizing Eqs. 8 to 14. First, in order to ensure we recover ideal MHD behavior appropriately, we choose to evolve Eq. 11 via a constrained transport [21] method with face-centered magnetic fields, as shown in Fig. 1.

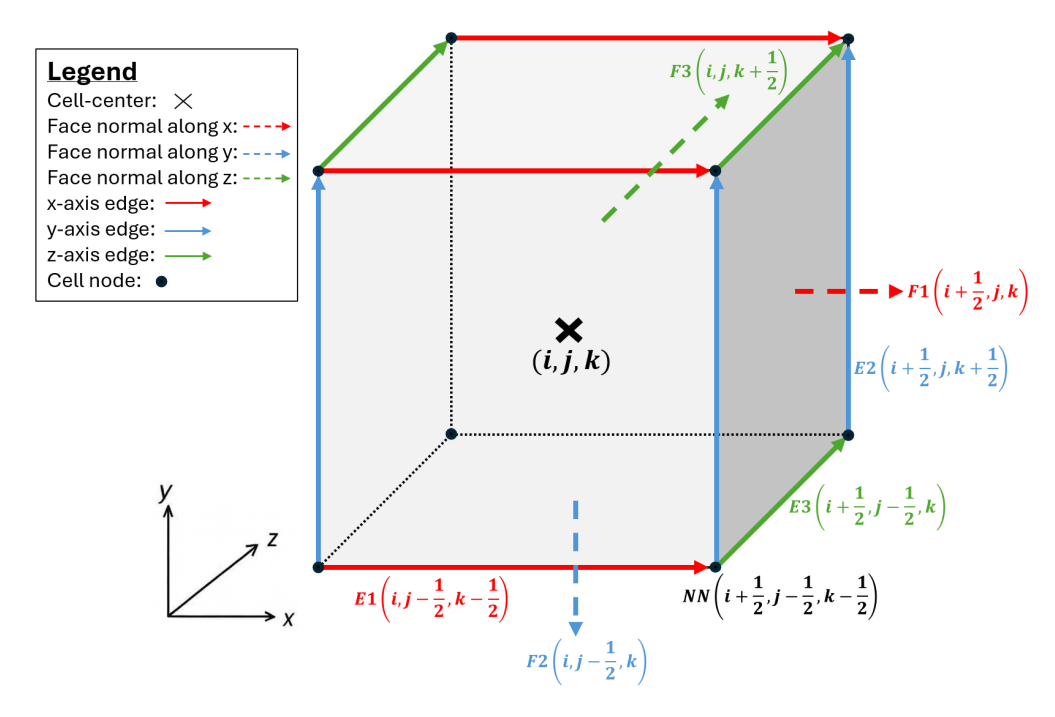


Figure 1: A 3D computational cell on a Cartesian grid is illustrated to indicate the positions of various field variables. The cell center is marked with an 'x', while the arrows normal to each cell face represent F1, F2, and F3, corresponding to faces with normal directions along the x, y, and z axes, respectively. The cell edges are shown by arrows labeled E1, E2, and E3, indicating edges oriented along the x, y, and z directions. The cell nodes are depicted as solid black dots and are denoted by NN. **B** is placed on the faces (F) while both **E** and **J** lie on the edges (E). The rest of the conserved variables are placed at the cell-center (i, j, k).

Second, spatial interpolation of variables should be high-order and minimized as they introduce additional errors. For instance, **E** should be placed at the cell edges so that it can be used to update the magnetic field together with  $\mathbf{u} \times \mathbf{B}$  without requiring spatial interpolation in Eq. 11. Furthermore, taking its curl to update the face-centered magnetic field will preserve  $\nabla \cdot \mathbf{B} \approx 0$  similar to constrained transport method. As for **J**, it should be placed at the cell-edges since it will be updated together with **E** through implicit source terms and therefore, both must be co-located to be consistent. However, spatial interpolation of the non-ideal MHD ( $\mathbf{E} + \mathbf{u} \times \mathbf{B}$ ) and relativistic source terms ( $\mathbf{J} - \nabla \times \mathbf{B}$ ) from cell edges to cell center in Eqs. 9 and 10 are still required.

To compute the intercell numerical inviscid flux, the local Lax-Friedrichs (LLF) Riemann solver [22] can be applied for all the variables. For improved accuracy, the convective components from the left-hand side of Eqs. 8 to 11 can be obtained using the HLLD Riemann solver [23] instead. Operator splitting is applied to **E** and **J** source terms while the rest of the source terms are explicitly updated together with the flux. The algorithm for solving Eqs. 17-21 and 15-16 is detailed as follows,

## Algorithm 1: Finite Volume scheme for XMHD equations

- 1: Initialize cell-centered conserved variables  $\mathbf{U}^n$  and face-centered magnetic field  $\mathbf{B}^n$ .
- 2: Initialized edge-centered **E** and **J** using the ideal MHD Riemann solver  $(-\mathbf{u} \times \mathbf{B}|^n)$  and  $\nabla \times \mathbf{B}^n$ , respectively.

## Predictor stage:

- 3: Convert conserved variables from  $\mathbf{U}^n$  to primitive variables  $\mathbf{V}^n$ .
- 4: Compute and store numerical interface fluxes with Riemann solver using  $\mathbf{V}^n$ ,  $\mathbf{B}^n$ ,  $\mathbf{E}^n$  and  $\mathbf{J}^n$ .
- 5: Compute and store ideal MHD's electromotive forces (EMFs) at cell edges using the **B**-component from the interface fluxes through constrained transport method.
- 6: Interpolate and store the **J**-component interface fluxes to the cell nodes.
- 7: Compute and store explicit source terms from Eqs. 17 to 21 using current values including  $-\mathbf{u} \times \mathbf{B}|^n$  obtained from Step 5.
- 8: Update edge-centered  $\mathbf{E}^n$  using the curl of the face-centered  $\mathbf{B}^n$  to  $\mathbf{E}^{**}$  like in Eq. 65.
- 9: Update edge-centered  $\mathbf{J}^n$  to  $\mathbf{J}^{**}$  using the divergence of its node fluxes and this is detailed in Sect. 3.7.
- 10: Update face-centered  $\mathbf{B}^n$  to  $\mathbf{B}^*$  by taking the curl of edge-centered EMFs computed from Step 5 and explicit source term from Step 7, similar to constrained transport method.
- 11: Advance remaining cell-centered variables from  $\mathbf{U}^n$  to intermediate (predictor) state  $\mathbf{U}^*$  using the computed fluxes and explicit source terms.
- 12: Recompute primitive variables  $V^*$  from the updated intermediate conserved variables  $U^*$  earlier since the implicit source term update is split from the flux and explicit source term update.
- 13: Recompute and store  $-\mathbf{u}^* \times \mathbf{B}^*$  at the edge using ideal MHD Riemann solver and constrained transport method with  $\mathbf{V}^*$  and  $\mathbf{B}^*$  as the inputs.

## Implicit source term update:

14: Solving for  $J^*$  requires a semi-implicit time advancement to the source terms in Eqs. 15 and 16 which yields the following spatially local linear algebraic equations for  $E^*$  and  $J^*$ ,

$$\mathbf{E}^* = \mathbf{E}^{**} - \Delta t \frac{c^2}{v^2} \mathbf{J}^* \tag{27}$$

$$\mathbf{J}^* = \mathbf{J}^{**} + \Delta t \frac{L_0^2 n^*}{\lambda_e^2} \left( \mathbf{E}^* + \mathbf{u}^* \times \mathbf{B}^* - \frac{\lambda_i}{L_0 n^*} \mathbf{J}^* \times \mathbf{B}^* - \underline{\eta}^* \mathbf{J}^* \right), \tag{28}$$

where  $\underline{n}^* = \operatorname{diag}(n_x^*, n_y^*, n_z^*)$ ,  $\underline{\eta}^* = \operatorname{diag}(\eta_x^*, \eta_y^*, \eta_z^*)$  and  $\mathbf{u}^* \times \mathbf{B}^*$  is obtained from Step 13. Note that  $\mathbf{E}^{**}$  and  $\mathbf{J}^{**}$  are the intermediate values before implicit source term update. Substituting  $\mathbf{E}^*$  from Eq. 27 into Eq. 28 gives a 3 by 3 linear system

$$AJ^* = b^*, \tag{29}$$

where k = x, y, z corresponds to values at each edge and

$$\mathbb{A} = \begin{bmatrix} \alpha_x & \frac{\lambda_i}{L_0 n_x^*} B_z^* & -\frac{\lambda_i}{L_0 n_x^*} B_y^* \\ -\frac{\lambda_i}{L_0 n_y^*} B_z^* & \alpha_y & \frac{\lambda_i}{L_0 n_y^*} B_x^* \\ \frac{\lambda_i}{L_0 n_z^*} B_y^* & -\frac{\lambda_i}{L_0 n_z^*} B_x^* & \alpha_z \end{bmatrix}, \qquad \mathbf{b}^* = \frac{\boldsymbol{\tau} \boldsymbol{\tau}^{\mathbb{I}}}{\Delta t} \mathbf{J}^{**} + \mathbf{E}^{**} + \mathbf{u}^* \times \mathbf{B}^*,$$

$$\alpha_k = \frac{\tau_k^2}{\Delta t} + \Delta t \frac{c^2}{v^2} + \eta_k^*, \qquad \tau_k = \frac{\lambda_e}{L_0 \sqrt{n_k^*}}.$$

A can then be explicitly inverted, allowing  $J^*$  to be solved analytically according to Eq. 28. Here Gaussian elimination with partial pivoting [24] is used to solve Eq. 29 in case A becomes poorly-conditioned for improved numerical stability. Additionally, directional splitting of implicit source term update is required due to the Hall term which is explained further in Sect. 3.5.

15: Solve for  $\mathbf{E}^*$  using  $\mathbf{J}^*$  computed from previous step using Eq. 27.

### Corrector stage:

- 16: Recompute fluxes, source terms, and EMFs at the intermediate state like in the previous steps from 3 to 15.
- 17: Apply the RK2 (Heun) corrector step to obtain  $\mathbf{U}^{n+1}$ ,  $\mathbf{B}^{n+1}$ ,  $\mathbf{E}^{n+1}$  and  $\mathbf{J}^{n+1}$ .

## Post-time step update:

- 18: Update simulation time:  $t^{n+1} = t^n + \Delta t$
- 19: Apply boundary conditions.
- 20: Repeat steps 3 to 19 until simulation end time is reached.

The explicit components of the time evolution can also be performed using a higher-order strong-stability preserving (SSP) integrator like the 3rd-order Shu-Osher Runge-Kutta method [25] instead of the SSP-RK2 method used here.

## 3.1. Slope limiter

The source term can induce fast dynamics, such as high frequency Whistler wave oscillations caused by Hall effect. Since the Hall effect is larger at low density (as will be shown later in Eq. 79 where the whistler wave scales as  $\frac{1}{n_e}$ ), these rapid variations may not be accounted for when computing the timestep for each update. To prevent the accumulation of numerical artifacts that could eventually contaminate the solution, such oscillations should be damped out. This is done by introducing an additional density-dependent slope limiter together with a total variation diminishing (TVD) slope limiter, which is used to eliminate spurious oscillations from each flux update. The resulting cell-interface primitive variables reconstruction is

$$\mathbf{U}_{i+\frac{1}{2}}^{L} = \mathbf{U}_{i} + \frac{1}{2}\psi(n_{i})\phi(\mathbf{r}_{i})\Delta\mathbf{U}_{i}, \quad \mathbf{U}_{i+\frac{1}{2}}^{R} = \mathbf{U}_{i+1} - \frac{1}{2}\psi(n_{i})\phi(\mathbf{r}_{i})\Delta\mathbf{U}_{i+1}, \tag{30}$$

where  $\phi(\mathbf{r}_i)$  is the TVD slope limiter like monotonized central (MC) [26] which depends on the ratio of the upstream to downstream slope.  $\psi(n_i)$  is an additional density-dependent slope limiter which depends on the local density  $n_i$ . This slope limiter must be equal to 1 at continuum limit and approach 0 as the density decreases towards the kinetics limit. The rationale for this is to increase the flux diffusivity to damp out small but fast oscillating waves that would otherwise contaminate the solution if not resolved. This effect becomes more significant as the flow density decreases. A simplified model for this is a sigmoid function which restrict the gradient of density away from continuum limit as follows,

$$\psi(n_i) = \left(1 + \exp\left(\frac{\left(\frac{\lambda_0}{\Delta x}\right)^3 - n_i}{L_0}\right)\right)^{-1},\tag{31}$$

where  $\left(\frac{\lambda_0}{\Delta x}\right)^3$  is a free parameter and from the shock tube problem, 0.005 is a suitable value. This can be seen akin to a local Knudsen number of around 0.17 which lies in the transition regime away from the continuum limit. Therefore, as the flow density decreases and approaches the molecular limit, the above limiter approaches zero, giving rise to a 1st-order diffusive flux to stabilize the solution by damping out small amplitude but high frequency oscillations. Future work could be focused on a more rigorous density-dependent slope limiter without any free parameter.

## 3.2. Primitive form for flux Jacobian

We can compute the signal speeds of the XMHD model by computing the eigenvalues of the flux Jacobian. Consider the Jacobian of the conserved system without the source term from Eqs. 15 - 21,

$$\frac{\partial \mathbf{U}}{\partial t} + \mathbb{A}(\mathbf{U}) \frac{\partial \mathbf{U}}{\partial x} = \mathbf{0}, \quad \mathbb{A}(\mathbf{U}) = \frac{\partial \mathbf{F}}{\partial \mathbf{U}}$$
(32)

which can be written in primitive form

$$\frac{\partial \mathbf{V}}{\partial t} + \mathbb{A}_p(\mathbf{V}) \frac{\partial \mathbf{V}}{\partial x} = \mathbf{0},\tag{33}$$

where the primitive variables for 1D XMHD are  $\mathbf{V} = [\rho, u, v, w, B_y, B_z, p, E_x, E_y, E_z, J_x, J_y, J_z, P_e]^T$  and the flux Jacobian is

where

$$C_1 = (\gamma - 1)P_e\rho u + (1 - \gamma)P_e\rho \left(u - \frac{J_0}{en_0 v} \frac{J_x}{Z\rho}\right) + P_e \frac{J_0}{en_0 v} \frac{J_x}{Z\rho^2}$$
(34)

$$C_2 = (\gamma - 1)P_e \rho^2 + P_e. (35)$$

The Jacobian can then be written as four sub-blocks,

$$\mathbb{A}_p = \begin{bmatrix} \underline{A} & \underline{0} \\ \underline{B} & \underline{C} \end{bmatrix}. \tag{36}$$

This allows one to obtain the eigenvalues of the Jacobian much more easily since it is a block lower-triangular matrix.

$$det(\lambda \mathbb{I} - \mathbb{A}_p) = det(\lambda \mathbb{I} - \underline{A}) det(\lambda \mathbb{I} - \underline{C}). \tag{37}$$

The eigenvalues corresponding to ideal MHD are preserved since they are decoupled from the additional equations from XMHD. The characteristic speeds for the flux Jacobian are

$$\lambda_{1} = u - c_{f}, \qquad \lambda_{2} = u - c_{a}, \qquad \lambda_{3} = u - c_{s}, \qquad \lambda_{4} = u,$$

$$\lambda_{5} = u + c_{s}, \qquad \lambda_{6} = u + c_{a}, \qquad \lambda_{7} = u + c_{f}, \qquad \lambda_{11} = u - \frac{\lambda_{i} J_{x}}{L_{0} \rho},$$

$$\lambda_{12} = u - \frac{\lambda_{i} J_{x}}{L_{0} \rho}, \qquad \lambda_{13} = u + c_{m}, \qquad \lambda_{14} = u + c_{p},$$
(38)

where  $c_f$  and  $c_s$  are the fast and slow magnetosonic speeds, respectively:

$$c_f^2 = \frac{1}{2} \left( a^{*2} + \sqrt{a^{*4} - 4a^2 b_x^2} \right), \tag{39}$$

$$c_s^2 = \frac{1}{2} \left( a^{*2} - \sqrt{a^{*4} - 4a^2 b_x^2} \right), \tag{40}$$

with

$$a^2 = \frac{\gamma p}{\rho}, \quad \mathbf{b} = \frac{1}{\sqrt{\rho}}(B_x, B_y, B_z), \quad a^{*2} = a^2 + |\mathbf{b}|^2,$$
 (41)

and  $c_a$  is the Alfvén speed,

$$c_a = \frac{B_x}{\sqrt{\rho}}. (42)$$

There are three new wavespeeds  $(\lambda_{11} = \lambda_{12}, \lambda_{13}, \lambda_{14})$  where

$$c_{m} = \frac{3}{2}u - \frac{\lambda_{i}J_{x}}{L_{0}\rho} - \frac{J_{0}}{2en_{0}v}\frac{J_{x}}{Z\rho} - \sqrt{\left(\frac{J_{0}J_{x}}{2en_{0}vZ\rho} - \frac{\lambda_{i}J_{x}}{L_{0}\rho}\right)^{2} + \frac{J_{0}P_{e}m_{i}L_{0}}{en_{0}vZ\rho m_{e}\lambda_{i}}}$$
(43)

$$c_p = \frac{3}{2}u - \frac{\lambda_i J_x}{L_0 \rho} - \frac{J_0}{2en_0 v} \frac{J_x}{Z \rho} + \sqrt{\left(\frac{J_0 J_x}{2en_0 v Z \rho} - \frac{\lambda_i J_x}{L_0 \rho}\right)^2 + \frac{J_0 P_e m_i L_0}{en_0 v Z \rho m_e \lambda_i}}.$$
 (44)

Note that v here is the constant used to non-dimensionalize velocity. Additionally, the characteristic speed does not depend on the speed of light which means that the timestep is not overly restricted. However, the source term may introduce signal speeds much faster than the ones above, especially at near vacuum where the signal speed will approach the speed of light. A safer approach will be to use the electron sound speed which is also used in this code as was generally found to be larger than the above three new wavespeeds in our experiments. The wavespeeds based on the electron sound speeds are

$$\lambda_{es} = u \pm \sqrt{\frac{m_i}{m_e}} a. \tag{45}$$

Note that the explicit source terms depend on  $\mathbf{E}$  and  $\mathbf{J}$  which are implicitly updated by the diffusive backward Euler to relax the stiff source term to the equilibrium value where the characteristic speeds of the flux Jacobian becomes more important. Moreover, the relaxation accounts for the speed of light according to Eqs. 51 which shows that larger  $\Delta t$  results in faster relaxation since more higher-order terms are damped out. However, these are not sufficient and thus, density-dependent slope limiters are required for the shock tube problem to further damp out small and fast oscillations. More rigorous analysis and testing will be needed in future.

# 3.3. Relaxation of stiff source term

The extended MHD can be seen as deviation from the equilibrium values of  $\mathbf{E}_0 = -\mathbf{u} \times \mathbf{B}$  and  $\mathbf{J}_0 = \nabla \times \mathbf{B}$  derived from ideal MHD. To show relaxation and neglecting Hall term here to simplify analysis, the implicit source term update can be written as the following discretized linear differential equations

$$\mathbf{J}^{n+1} = \mathbf{J}^* + \frac{\Delta t}{\epsilon_I} (\mathbf{E}^{n+1} - \mathbf{E}_0 - \eta \mathbf{J}^{n+1})$$
(46)

$$= \mathbf{J}^{n} + \Delta t \nabla \cdot \mathbb{J} + \frac{\Delta t}{\epsilon_{J}} (\mathbf{E}^{n+1} - \mathbf{E}_{0} - \eta \mathbf{J}^{n+1})$$
(47)

$$\mathbf{E}^{n+1} = \mathbf{E}^* + \frac{\Delta t}{\epsilon_E} (\mathbf{J}_0 - \mathbf{J}^{n+1}) \tag{48}$$

$$= \mathbf{E}^n + \Delta t \nabla \times \mathbb{E} + \frac{\Delta t}{\epsilon_E} (\mathbf{J}_0 - \mathbf{J}^{n+1}), \tag{49}$$

where  $\mathbb{E} = \frac{c^2}{v^2}\mathbf{B}$  and  $\mathbb{J}$  is the convective flux from Eq. 66 while the relaxation parameters are  $\epsilon_E = \frac{v^2}{c^2}$  and  $\epsilon_J = \frac{\lambda_e^2}{L_0^2 n}$ . If  $\Delta t << \epsilon_E$  and  $\Delta t << \epsilon_J$ ,  $\mathbf{J}^*$  and  $\mathbf{E}^*$  will be advanced in time by backward Euler equation. If  $\Delta t >> \epsilon_E$  and  $\Delta t >> \epsilon_J$ , the above equations will reduce to

$$\mathbf{J}^{n+1} = \mathbf{J}_0 \; ; \; \mathbf{E}^{n+1} = \mathbf{E}_0 + \eta \mathbf{J}_0.$$
 (50)

where  $\mathbf{J}^{n+1}$  and  $\mathbf{E}^{n+1}$  are independent of electron inertia and pressure effects. For ideal MHD,  $\eta$  is very small and this will render the non-ideal and relativistic source terms to zero, recovering the ideal MHD solver.

Solving for  $\mathbf{J}^{n+1}$  and  $\mathbf{E}^{n+1}$  using the above equations (directionally unsplit here for simplicity) and expanding the solution to second order in  $\frac{\epsilon_J}{\Delta t}$  and  $\frac{\epsilon_E}{\Delta t}$  yields corrections to the equilibrium states  $\mathbf{E}_0$  and  $\mathbf{J}_0$ . These deviations are of order  $\frac{\epsilon_J}{\Delta t}$  or  $\frac{\epsilon_E}{\Delta t}$  and arise from non-ideal effects.

$$\mathbf{J}^{n+1} \approx \left(1 - \frac{\eta \epsilon_E}{\Delta t} + \frac{\epsilon_E (\eta^2 \epsilon_E - \epsilon_J)}{\Delta t^2}\right) \mathbf{J}_0 + \frac{\epsilon_E}{\Delta t} \left(\frac{\eta \epsilon_E}{\Delta t} - 1\right) \left(\mathbf{E}_0 - \mathbf{E}^*\right) + \frac{\epsilon_J \epsilon_E}{\Delta t^2} \mathbf{J}^*$$
 (51)

$$\mathbf{E}^{n+1} \approx \mathbf{E}_{0} + \eta \mathbf{J}_{0} + \frac{\epsilon_{J}}{\Delta t} \left( 1 - \frac{\eta \epsilon_{E}}{\Delta t} \right) (\mathbf{J}_{0} - \mathbf{J}^{*}) + \frac{\epsilon_{E}}{\Delta t} \left( \frac{\eta^{2} \epsilon_{E}}{\Delta t} - \eta - \frac{\epsilon_{J}}{\Delta t} \right) (\mathbf{E}_{0} - \mathbf{E}^{*})$$

$$+ \mathbf{J}_{0} \left( -\frac{\eta^{2} \epsilon_{E}}{\Delta t} + \frac{\eta^{3} \epsilon_{E}^{2}}{\Delta t^{2}} - \frac{\epsilon_{e} \epsilon_{J} \eta}{\Delta t^{2}} + \frac{\epsilon_{J}^{2}}{\eta \Delta t^{2}} \right)$$

$$(52)$$

# 3.4. Temporal order of accuracy

The temporal update of the current algorithm uses operator splitting of explicit and implicit components at each substage. The explicit second-order Runge–Kutta (RK2) method achieves second-order accuracy for the unsplit explicit flux and source term updates but only first-order accuracy for the implicit source term update. As a result, the overall temporal accuracy remains first order. A formal proof of the temporal accuracy is shown below and a slightly more general scheme (e.g., introducing  $\alpha$  and  $\gamma$ ) is used to avoid an over-determined system of equations.

$$U_1 = U^n - \alpha \frac{\Delta t}{\epsilon} R(U_1) \tag{53}$$

$$U_2 = U_1 - \tilde{\alpha} \Delta t D F(U_1) \tag{54}$$

$$U_3 = U_2 - \beta \frac{\Delta t}{\epsilon} R(U_3) - \gamma \frac{\Delta t}{\epsilon} R(U_1)$$
 (55)

$$U_4 = \xi U^n + \eta U_3 \tag{56}$$

$$U_5 = U_4 - \tilde{\beta} \Delta t D F(U_4) \tag{57}$$

$$U^{n+1} = U_5 - \mu \frac{\Delta t}{\epsilon} R(U^{n+1}), \tag{58}$$

where R(U) and DF(U) are the implicit and explicit update, respectively. The explicit source and flux are left unsplit to simplify the problem of finding a solution to this linear analysis. The advantage of operator splitting of implicit and explicit parts at each substage is that it ensures that the stiff source term relaxes to  $R(U) \approx 0$  which in the ideal MHD limit will preserve the specific form of the Ohm's law,  $\mathbf{E} \approx -\mathbf{u} \times \mathbf{B}$ . This will then be used to update the flux while the explicit non-ideal source term will go to zero. The above steps should ideally be combined such that they are 2nd-order accurate in the linear regime.

Applying Eqs. 53 - 58 to a linear system gives [27]

$$\partial_t U + AU + BU = 0, (59)$$

where A and B are constant matrices but A is treated implicitly. This gives the following exact solution at time  $t = \Delta t$ ,

$$U(\Delta t) = e^{-(A+B)\Delta t}U(0). \tag{60}$$

For 2nd-order of accuracy, the following condition must be imposed

$$(\mathcal{C}(\Delta t) - e^{-(A+B)\Delta t})U(0) = \mathcal{O}(\Delta t^3), \tag{61}$$

where C is the numerical scheme from Eqs. 53 - 58. This gives the following simultaneous equations that must be solved,

$$\xi + \eta = 1, \quad \tilde{\alpha}\eta + \tilde{\beta}\eta + \tilde{\beta}\xi = 1, \quad \eta(\alpha + \gamma + \beta) + \mu(\xi + \eta) = 1$$
 (62)

$$2\eta\tilde{\alpha}\tilde{\beta} = 1, \quad 2\mu(\tilde{\alpha}\eta + \tilde{\beta}\eta + \tilde{\beta}\xi) + 2\tilde{\alpha}\beta\eta = 1, \quad 2\eta(\tilde{\alpha}\alpha + \tilde{\beta}\alpha + \tilde{\beta}\gamma + \tilde{\beta}\beta) = 1, \tag{63}$$

$$\eta(\alpha^2 + \alpha\gamma + \beta\alpha + \beta\gamma + \beta^2) + \eta\mu(\alpha + \gamma + \beta) + \mu^2(\xi + \eta) = \frac{1}{2}.$$
 (64)

This gives an under-determined system with 7 equations with 8 unknowns to be solved. Satisfying Eq. 62 gives 1st-order accuracy while satisfying Eqs. 62-64 gives 2nd-order accuracy. The explicit RK2 method with operator splitting of implicit substage update has the following coefficients  $\left(\xi,\eta,\alpha,\mu,\beta,\gamma,\tilde{\alpha},\tilde{\beta}\right) = \left(\frac{1}{2},\frac{1}{2},0,\frac{1}{2},1,0,1,\frac{1}{2}\right)$  which only satisfies Eq. 62. Therefore, when non-ideal effects become more significant, the solution approaches 1st-order of accuracy temporally.

# 3.5. Directional splitting of implicit source term update

The Hall term contains the cross product  $(\mathbf{J} \times \mathbf{B})$  which must be treated carefully since the x, y and z components lie on different edges orthogonal to each other. One simply cannot just take the cross-product of these spatially-separated edge components which will lead to some spatial biasing that may lead to bad results especially when the non-ideal effects dominate. Instead, for n-dimensional spatial problem, the implicit update is done n times which is described as follows for 3D problem,

#### **Algorithm 2**: Directional splitting of implicit source term update

- 1: Interpolate density and electron pressure (required to compute Spitzer resistivity) from cell-center to the edge along x.
- 2: Interpolate face-centered  ${f B}$  to the edge.
- 3: Interpolate  $\mathbf{J}_{\perp}$  and  $\mathbf{E}_{\perp}$  to the edge along x.
- 4: Interpolate  $\mathbf{u} \times \mathbf{B}|_{\perp}$  obtained from the ideal MHD Riemann solver through constrained transport method to the edge along x.
- 5: Implicitly update  $J_x$ ,  $E_x$  using Eq. 29. This will also produce new  $\mathbf{J}_{\perp}$  and  $\mathbf{E}_{\perp}$  which lie along x-edge that are discarded.
- 6: Steps 1 to 5 are then repeated for edge along y and z using old **E** and **J** values before their implicit update.

Directional splitting of the implicit update means that the implicit source term update is no longer fully implicit which may affect the stability of the solver. Moreover, some values are discarded and the implicit update does not guarantee that  $\nabla \cdot \mathbf{J}$  remains small at the cell node for the quasi-neutrality assumption to hold. Future work will focus on directionally unsplit implicit source-term update, which may be important for preserving, or at least limiting the growth of  $\nabla \cdot \mathbf{J}$  at those locations.

3.6. Interpolation of variables across different topological elements Interpolation is required as the variables are all not co-located. For instance,

- B field lies on the cell faces, for example F1, F2, F3 from Fig. 1.
- E, J and  $-\mathbf{u} \times \mathbf{B}$  (obtained from ideal MHD Riemann solver through constrained transport method) fields lie on the cell edges, for example E1, E2, E3 from Fig. 1.
- The flux for **J** lies on cell nodes, for example NN from Fig. 1. This is obtained by interpolating the cell's interface flux obtained from the LLF Riemann solver to the cell nodes.

The rest of the variables lies at the cell center and their corresponding fluxes lie at the cell face. Here, simple arithmetic averaging is sufficient which is also applied for the constrained transport method implemented here to ensure divergence-free magnetic field.

# 3.7. Explicit update of edge-centered variables

The curl of face-centered magnetic field naturally maps to the edge which can then be directly used to update **E** as follows,

$$\frac{\partial \mathbf{E}}{\partial t} - \frac{c^2}{v^2} (\nabla \times \mathbf{B}) = 0 \tag{65}$$

However, the update of edge-centered J is less straightforward as the divergence of the flux in Eq. 66 indicates that the flux must be placed at the cell nodes.

$$\frac{\partial \mathbf{J}}{\partial t} + \nabla \cdot \left( \mathbf{u} \mathbf{J} + \mathbf{J} \mathbf{u} - \frac{\lambda_i}{L_0 n} \mathbf{J} \mathbf{J} - \frac{m_i L_0}{m_e \lambda_i} P_e \mathbb{I} \right) = 0, \tag{66}$$

The flux for **J** is first obtained from the LLF Riemann solver at the cell faces and then interpolated to the cell nodes. The divergence of the flux at the cell nodes is subsequently used to update the edge-centered **J** values. For instance, for  $J_x$  located at  $E1(i, j - \frac{1}{2}, k - \frac{1}{2})$  as shown in Fig. 2, the change in  $J_x$  due to the divergence of the parallel component of the convective flux can be computed directly by taking the finite difference of that component between the nodes  $NN(i-\frac{1}{2},j-\frac{1}{2},k-\frac{1}{2})$  and  $NN(i+\frac{1}{2},j-\frac{1}{2},k-\frac{1}{2})$ . However, the perpendicular components cannot be evaluated using the same two nodes, as they do not vary spatially along the y and z directions. Therefore, for example, for the y-contribution, the finite central difference must be applied twice: the first difference is taken between

 $NN(i-\frac{1}{2},j+\frac{1}{2},k-\frac{1}{2})$  and  $NN(i-\frac{1}{2},j-\frac{3}{2},k-\frac{1}{2})$ , and the second between  $NN(i+\frac{1}{2},j+\frac{1}{2},k-\frac{1}{2})$  and  $NN(i+\frac{1}{2},j-\frac{3}{2},k-\frac{1}{2})$ , as shown in Fig. 2. The average of these two finite central difference values is then used to update  $J_x$ . The same procedure applies for the z-contribution. Note that the stencil used for computing the perpendicular components of the convective flux is rather large while ignoring the center node which may affect numerical stability and this will be investigated further in future.

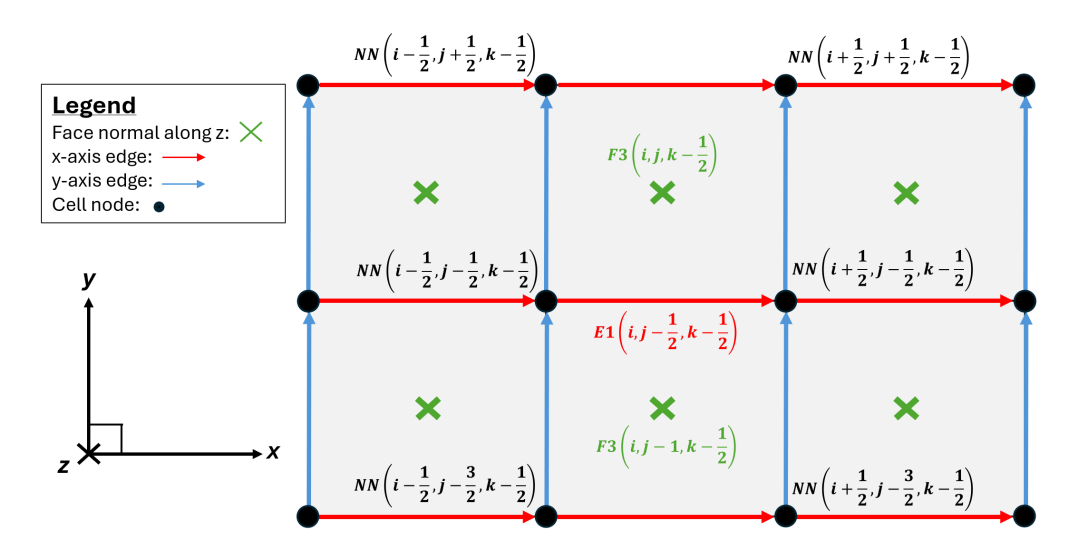


Figure 2: 2D diagram illustrating the faces F3 of six computational cells, with their normals directed into the paper along the z-axis. In this configuration, the faces  $F3(i,j,k-\frac{1}{2})$  and  $F3(i,j-1,k-\frac{1}{2})$  correspond to cell centers at (i,j,k) and (i,j-1,k), respectively. Each computational cell is bounded by edges that define its geometry: the horizontal arrows represent the edges E1, while the vertical arrows denote the edges E2. The edges E3, which align with the z-axis, are positioned at the cell nodes and point into the paper. The intersections of these edges are depicted as solid black dots to indicate cell nodes NN.

# 4. Numerical tests

This section focuses on testing the ability of the XMHD solver to address linear problems with known analytical solutions across different physical limits—ideal, resistive, and Hall MHD. For nonlinear problems involving discontinuities, the Brio–Wu shock tube test [28] is used as a stringent benchmark to assess the solver's capability to accurately capture nonlinear flow features and discontinuous structures. However, note that for conventional ideal MHD test, the MHD equations are typically written such that  $\mu_0 = 1$  [29] but this is not the case here which must be accounted for. Here, LLF Riemann solver will be employed for the ideal MHD components unless stated otherwise. This is because LLF Riemann solver is numerically more stable than HLLD Riemann solver especially at low densities where it is much more diffusive which will be shown in Sect. 4.3.

For the tests done here, Eqs. 8 to 14 will be non-dimensionalized to  $\mathbf{U} = U_0 \tilde{\mathbf{U}}$  where  $\tilde{\mathbf{U}}$  is the set of dimensionless variables while  $U_0$  is the set of dimensional normalization factors with the values in Table 1 unless stated otherwise:

TD 11 1 D C		1 C	1.	•	1
Table 1: Reference	naramatare	1190d to1	non-dim	angiana	lization
Table 1. Itelefelle	parameters	uscu ioi	. non-um	итыны	nzamon.

Parameter	Description	Value
$\overline{n_0}$	Reference number density	$6 \times 10^{28} \text{ m}^{-3}$
$t_0$	Reference time	100  ns
$L_0$	Reference length	$1 \mathrm{mm}$
$v_0$	Reference velocity	$10^4 \mathrm{m/s}$
$B_0$	Reference magnetic field	580 T
$E_0$	Reference electric field	$5.8 \times 10^{6} \text{ V/m}$
$J_0$	Reference current density	$4.6 \times 10^{11} \text{ A/m}^2$
$T_0$	Reference temperature	28  eV
$\sigma_0$	Reference conductivity	$\frac{1}{\mu_0 L_0 v_0} \Omega^{-1} \cdot \mathrm{m}^{-1}$

Unless stated otherwise, the material chosen here is Aluminium (Al) which has an ion mass number of 27 and an ionisation number (Z) of 3. As for the timestepping, it is done using the CFL condition (C),

$$\Delta t = C \frac{\Delta x}{\max(\lambda_i)} \tag{67}$$

where  $\lambda_i$  comes from Eqs. 38 and 45. 2nd-order Runge-Kutta time integration is employed for the explicit time-update of the conserved variables. 2nd-order piecewise-linear method (PLM) is used in conjunction with the density-dependent slope limiter from Eq. 31 and will then be referred to as modified PLM for brevity.

## 4.1. Brio-Wu shock tube problem

A common test case for ideal MHD solver is the magnetized shock tube with the following initial conditions,

$$(\rho, u_x, u_y, u_z, P, P_e, B_x, B_y, B_z) = \begin{cases} (1.000 \, \rho_0, \, 0, \, 0, \, 0, \, 0.10 \, \rho_0, \, 0.50 \, \rho_0, \, 0.75 \, \sqrt{\rho_0}, \, +\sqrt{\rho_0}, \, 0) \,, & \text{if } x \leq 0 \\ (0.125 \, \rho_0, \, 0, \, 0, \, 0, \, 0, \, 0.1 \, \rho_0, \, 0.05 \, \rho_0, \, 0.75 \, \sqrt{\rho_0}, \, -\sqrt{\rho_0}, \, 0) \,, & \text{if } x > 0 \end{cases}$$

For all the ideal MHD test cases, the resistivity is set to  $\eta = 10^{-8}$  [30] unless stated otherwise. XMHD solver will then be tested on  $\rho_0 = 1.0$  and  $\rho_0 = 0.01$ . Outflow boundaries are used here. The results of XMHD on Artemis are then compared to the ideal MHD solver on Athena++ to compare the discrepancy at low density regions due to non-ideal effects as shown in Fig. 4 and 5.

# 4.2. Ideal MHD linear wave test

In the ideal MHD limit, the XMHD is ideally expected to have 2nd-order convergence of L1 errors for the propagation of ideal MHD linear waves since RK2 and modified PLM are used here. The initial conserved variables state vector is [31]

$$q^{0} = \overline{q} + \epsilon R_{p} \cos\left(\frac{2\pi x_{1}}{\lambda}\right) \tag{68}$$

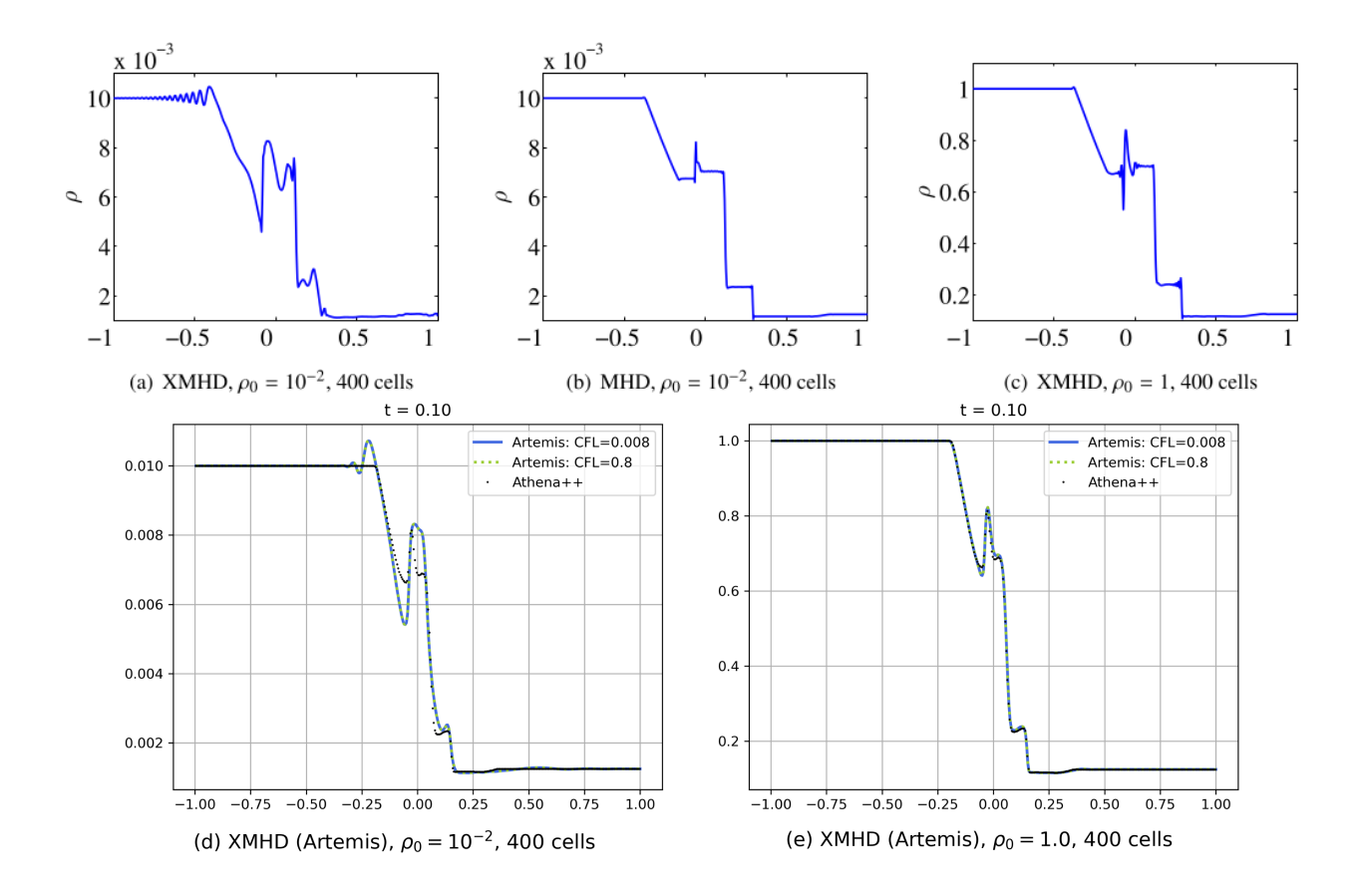


Figure 3: Brio-Wu shock tube solution from Zhao et. al. [16] using LLF Riemann solver at cell interface whereby the left figure (a) contains oscillation due to whistler wave introduced by Hall effect which is important at low density. However, the figure (c) on the right is unable to replicate the same solution as figure (b) at the ideal MHD limit. Figures (d) and (e) are produced using XMHD (LLF) on Artemis and compared against Athena++ ideal MHD solver (LLF) to show the increment of non-ideal effects at lower density. Different CFL numbers are also used to ensure that the solution is consistent at different time resolution.

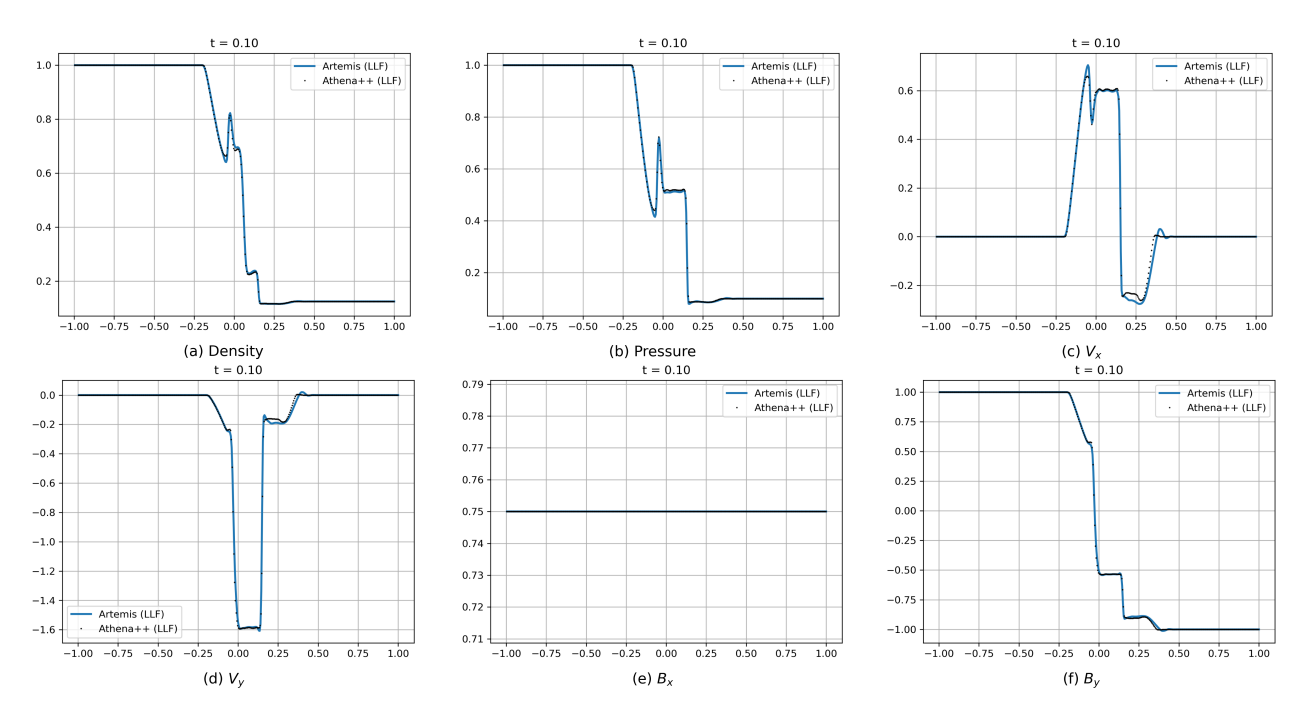


Figure 4: For the standard ideal MHD test case on shock tube, the XMHD (Artemis) is quite similar to ideal MHD (Athena++) but there is some discrepancy especially at lower-density region where non-ideal effects become more crucial.

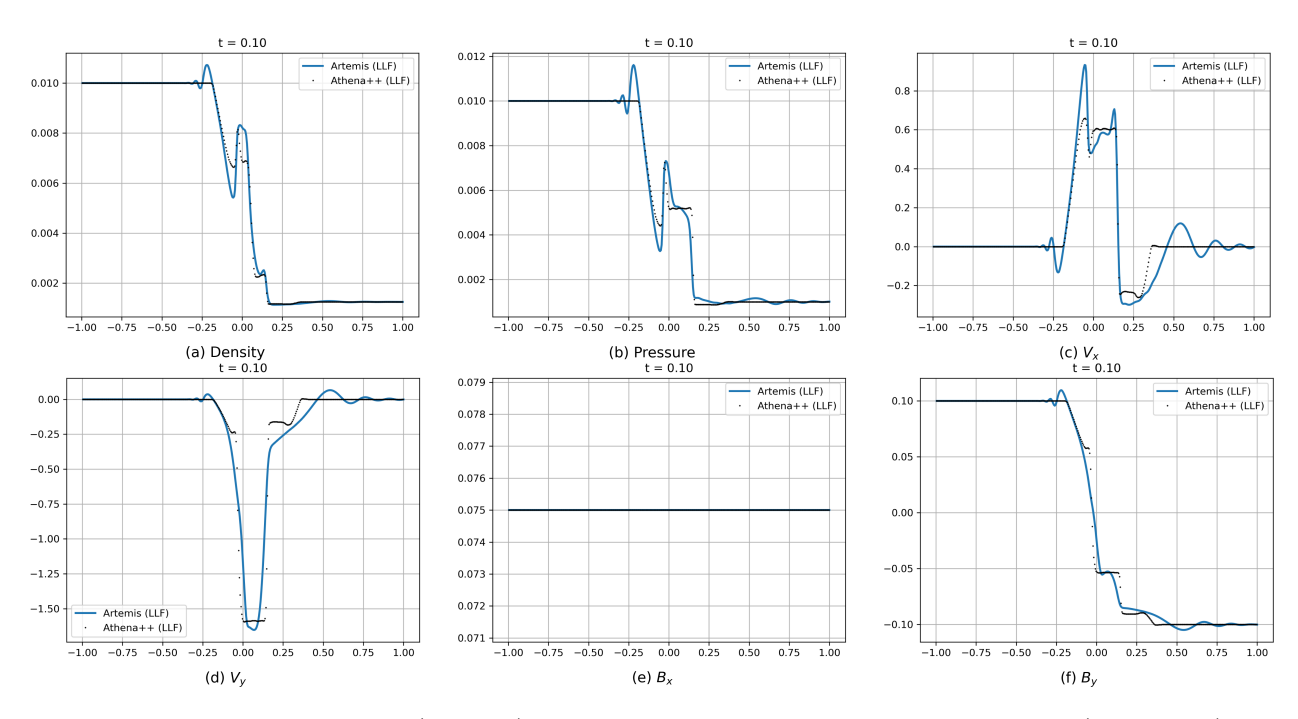


Figure 5: At low density, XMHD (Artemis) begins to deviate significantly from ideal MHD (Athena++) due to more significant non-ideal MHD effects.

where  $\bar{q}$  is the mean background state,  $\epsilon = 10^{-6}$  is wave amplitude and  $R_p$  is the right eigenvector in conserved variables for wave mode p. Here, density and pressure are set to 1 and  $\frac{1}{\gamma}$ , respectively. Velocity components are set to 0 except for  $v_x$  which is set to 1 for entropy mode test because Artemis run the test by wave period. After propagating each of the waves by a period, their L1 error w.r.t. their initial conditions for each component k of the conserved variables are computed as follows,

$$\delta q_k = \frac{1}{2N^2} \sum_{i} \sum_{j} |q_{i,j,k}^n - q_{i,j,k}^0|$$
(69)

by summing up over all the grid cells. The root-mean-square (RMS) error is then obtained by taking the norm of the above error vector

$$|\delta q| = \sqrt{\sum_{k} (\delta q_k)^2} \tag{70}$$

for each of the wave modes.

For 1D problem, a computational domain of [0,1] with grid resolutions of [16,32,64,128,256,512,1024] are tested. For multi-dimensional test problem of linear wave test, the linear wave is propagated such that it lies oblique to the grid and the coordinate transformation based on spherical coordinate is employed as follows

$$x = x_1 \cos \alpha \cos \beta - x_2 \sin \beta - x_3 \sin \alpha \cos \beta \tag{71}$$

$$y = x_1 \cos \alpha \sin \beta + x_2 \cos \beta - x_3 \sin \alpha \sin \beta \tag{72}$$

$$z = x_1 \sin \alpha + x_3 \cos \alpha \tag{73}$$

For 2D problem, it is done on a computational domain of  $[0, 2.236068] \times [0, 1.118034]$  with grid resolutions along x ranging from [16, 32, 64, 128, 256, 512].

As expected, the results in Fig. 6a show that without Hall and resistive terms, the coupling of ideal MHD and other components through the implicit source term update is correct in ensuring that  $\mathbf{E} \approx -\mathbf{u} \times \mathbf{B}$  due to the 2nd-order convergence from employing modified PLM and RK2 time integration. However, the entropy wave ceases to exhibit second-order convergence at very fine resolutions. This may result from the solver not sufficiently relaxing towards the ideal MHD limit as the grid resolution increases. Consequently,  $\mathbf{J}$  does not achieve second-order convergence towards  $\nabla \times \mathbf{B}$  at higher resolutions, causing the momentum source term to fail to converge to zero and thereby contaminating the entropy wave. For instance, when a different  $L_0$  is used such that  $\epsilon_J$  is smaller, as shown in Table 2,  $\mathbf{J}$  converges more rapidly towards  $\nabla \times \mathbf{B}$ . This behavior is evident in Fig. 6b, where using  $L_0 = 10^{-2}$  leads to second-order convergence, unlike the original case with  $L_0 = 10^{-3}$  at high resolution.

However, increasing  $L_0$  to reduce  $\epsilon_J$  is not ideal either, as it simultaneously increases  $\epsilon_E$ , making it more difficult for the displacement current to approach zero. This can also be observed in Fig. 6b, where  $L_0 = 10^{-1}$  yields the smallest  $\epsilon_J$  but the largest  $\epsilon_E$ , thus generally

have the largest RMS error, particularly at low resolutions. Therefore, an optimal choice of  $L_0$  is required to ensure that both  $\epsilon_E$  and  $\epsilon_J$  remain sufficiently small for the problem at hand. This balance will be investigated further in future work. As mentioned earlier, while non-dimensionalizing the equations, ensuring that  $\frac{B_0^2}{\mu_0 n_0 m_i v^2} \approx 1$  does not always yield the best results (e.g.,  $L_0 = 10^{-3}$  vs  $L_0 = 10^{-2}$  here), but this scaling will be adopted throughout the remainder of the paper for simplicity and consistency with previous studies.

	$L_0 = 10^{-3}$	$L_0 = 10^{-2}$	$L_0 = 10^{-1}$
$\epsilon_E$	$1.11 \times 10^{-9}$	$1.11 \times 10^{-7}$	$1.11 \times 10^{-5}$
$\epsilon_J$	$4.71 \times 10^{-10}$	$4.71 \times 10^{-12}$	$4.71 \times 10^{-14}$
$\frac{B_0^2}{\mu_0 n_0 m_i v^2}$	$9.95 \times 10^{-1}$	$9.95 \times 10^{-3}$	$9.95 \times 10^{-5}$

Table 2: Different relaxation parameters and explicit source term coefficient at different  $L_0$ .

Note that from Fig. 6a, entropy wave retains the same convergence order with or without the Hall and/or resistive term as it is not specific to ideal MHD. When Hall or resistive terms are involved, not all the waves have 2nd-order convergence especially for slow wave which gets worse at higher resolution when resistivity is involved. The deviation of 2nd-order convergence may also be a result of the Hall term which makes the phase speeds of waves wavenumber-dependent [32] and increasing resolution increases the Hall effect on the solution. Since Hall and resistive terms impede 2nd-order convergence for ideal MHD linear wave test, they will be turned off for multidimensional linear wave test like in Fig. 7 where 2nd-order convergence is expected.

# 4.3. Field Diffusion

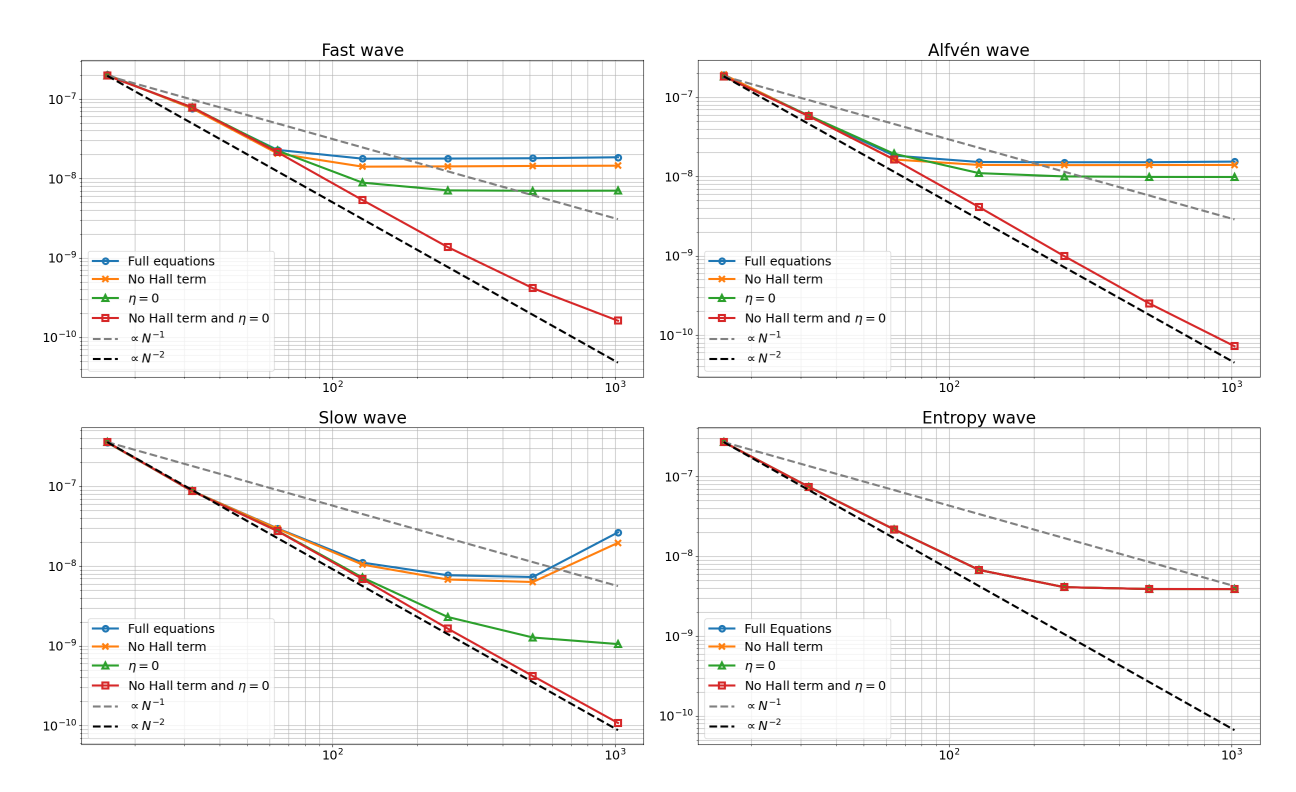
To test the resistive component of the XMHD, it is used to diffuse magnetic field with a n-dimensional Gaussian distribution as it has an analytical solution as follows [33]

$$\mathbf{G}(x, y, z, t) = \frac{A}{\sqrt{4\pi\eta^*(t_0 + t)^n}} \exp\left[-\frac{x^2 + y^2 + z^2}{4\eta^*(t_0 + t)}\right]$$
(74)

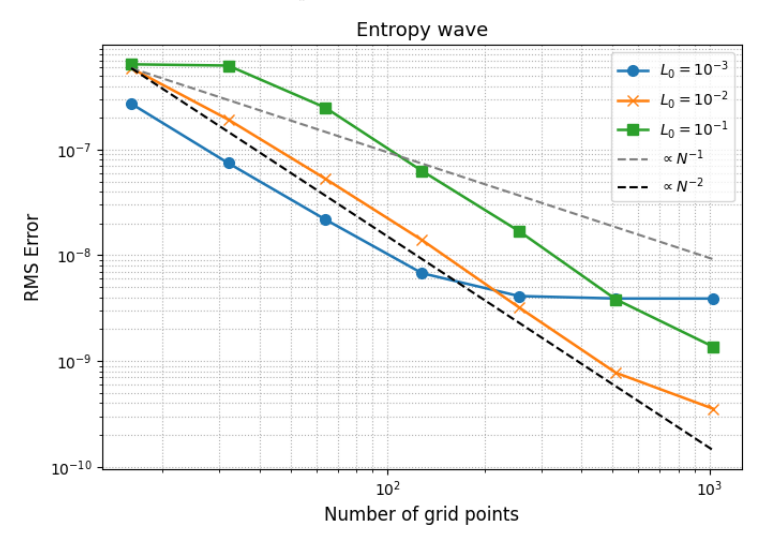
where n is the number of dimensions of the problem and  $\eta^* = \eta \sigma_0$  is the dimensionless resistivity used in the GOL equation. Here  $t_0$  is taken as 0.5 and the problem is evolve to  $t_f = t_0 + 2$ . For 1D tests, the L1 error of the result is computed as

$$L_{1,\xi} = \sum_{i=1}^{N} |\xi_i - \xi_{exact}| \Delta x \tag{75}$$

where  $\xi_i$  and  $\xi_{exact}$  are the numerical and exact solution at grid cell i, respectively. The problem is set up on a computational domain of [-6,6] with grid resolution of N = [32,64,128,256,512,1024,2048,4096]. The density and pressure are set to 1 while the velocities are set to 0 across the whole domain.  $B_x$  and  $B_z$  are set to 0 while  $B_y$  is initialized using the Gaussian distribution from Eq. 74. The dimensional resistivity is set



(a) To test for 2nd-order convergence in the ideal MHD limit, the code is tested by (i) using the full equations, (ii) setting Hall term to zero and, (iii) setting resitivity to zero and (iv) setting both Hall and resistive terms to zero. Only entropy wave is independent of the Hall or resistive terms as it is not specific to ideal MHD.



(b) Since entropy wave did not fully converge to 2nd-order especially at high resolution, a different  $L_0$  is used to ensure that the XMHD solver is able to relax sufficiently to the ideal MHD limit for 2nd-order convergence. Note that when different  $L_0$  is used, the background flow velocity and computational domain must be adjusted such that they are all consistent dimensionally.

Figure 6: For 1D problem at grid resolution of [16, 32, 64, 128, 256, 512, 1024].

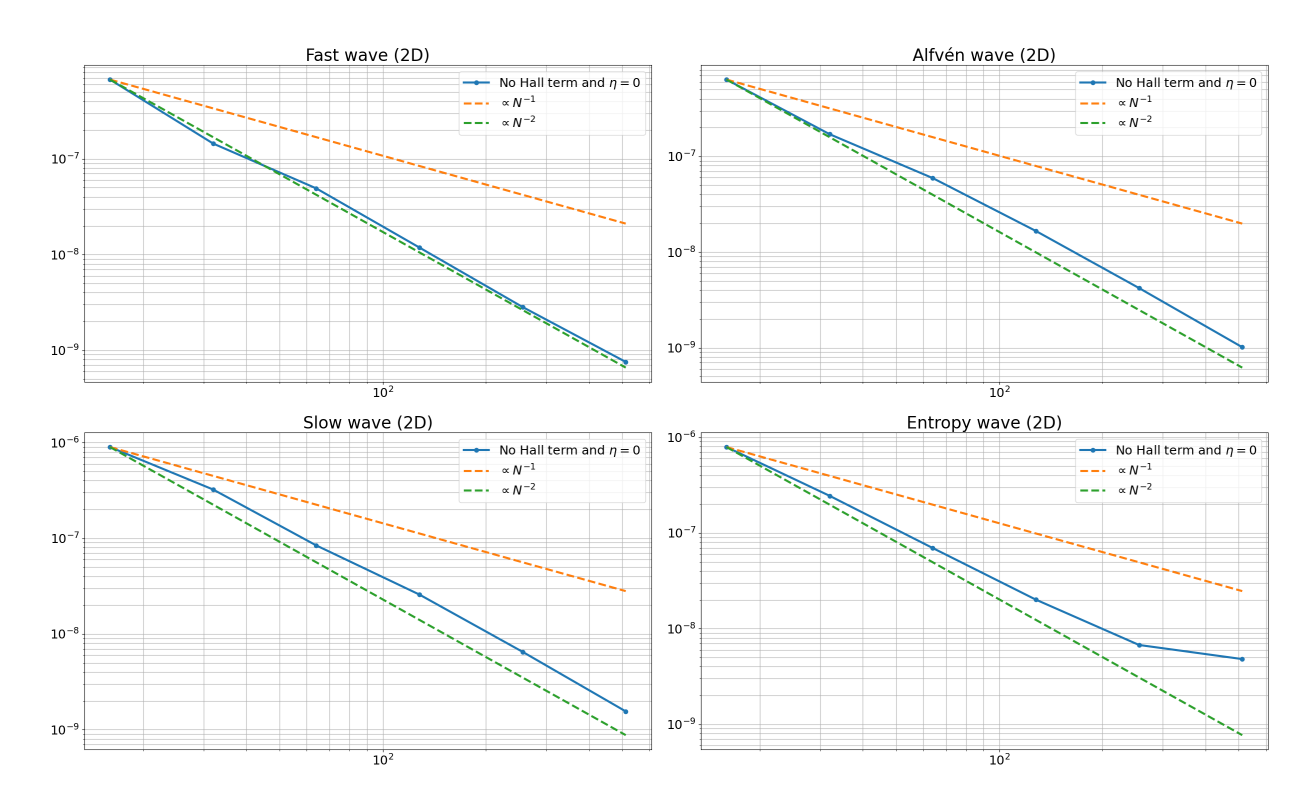


Figure 7: For 2D problem, the code is tested by setting both Hall and resistive terms to zero. 2nd-order convergence is expected since modified PLM and RK2 time integration are used.

to  $\eta=10^{-6}$  while the amplitude from Eq. 74 is set to  $A=10^{-6}$ . Interestingly, from the left diagram in Fig. 8, the algorithm has 2nd-order of convergence with increasing grid resolution instead of 1st-order from the implicit source term update.  $\rho_0$  is also varied to illustrate the deviation from resistive MHD as Hall term and electron inertia effects become more important at lower density, causing LLF solver to be more diffusive. However, HLLD becomes less diffusive which may also make it less stable than using LLF Riemann solver like in the low-density shocktube problem earlier.

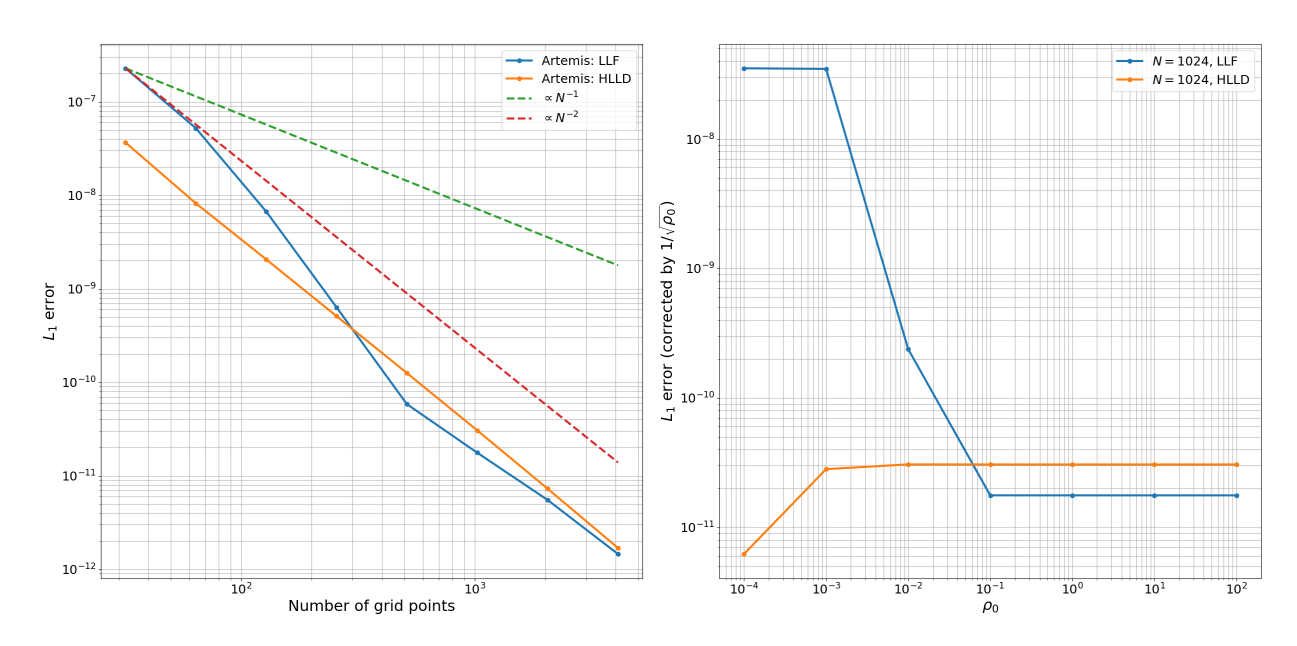


Figure 8: To test for order of convergence in 1D field diffusion problem, several grid resolution and their L1 error norms at t = 2.5 are plotted here.

# 4.4. 2D Huba's Hall drift problem

To test the algorithm in the limit where the Hall term dominates resistive and ideal effects, it is crucial to consider the two wave modes (e.g., Whistler and Hall drift waves) associated with the Hall term. For instance, the GOL can be simplified by assuming  $L_0 >> \frac{c}{\omega_{pe}}$ ,  $L_0 >> \rho_e$  and  $\eta \to 0$  where  $\omega_{pe}$  and  $\rho_e$  are the electron plasma frequency and electron Larmor radius, respectively. This allows one to neglect the electron inertia, electron pressure and resistive term, reducing to the simplified Ohm's law

$$\mathbf{E} = -\mathbf{u} \times \mathbf{B} + \frac{1}{n_e e} \mathbf{J} \times \mathbf{B} \tag{76}$$

where the final term is the Hall term which decouples ion and electron motion on ion inertial length scales  $L < c/\omega_{pi}$  where  $\omega_{pi} = \frac{4\pi n_i e^2}{m_i}$  is the Hydrogen ion plasma frequency which is used for this problem. This will reduce Eq. 20 to

$$\frac{\partial \mathbf{B}}{\partial t} - \nabla \cdot (\mathbf{B}\mathbf{u} - \mathbf{u}\mathbf{B}) = -\nabla \times \left(\frac{1}{n_e e}\mathbf{J} \times \mathbf{B}\right)$$
 (77)

Assuming stationary ( $\mathbf{u} = 0$ ) and neutralizing background, the above equation simplifies to

$$\frac{\partial \mathbf{B}}{\partial t} = -\nabla \times \left( \frac{1}{n_e e} \mathbf{J} \times \mathbf{B} \right) \tag{78}$$

$$= -\frac{1}{n_e e} \nabla \times (\mathbf{J} \times \mathbf{B}) + \frac{1}{n_e^2 e} \nabla n \times (\mathbf{J} \times \mathbf{B})$$
 (79)

where the first and second terms correspond to whistler and Hall drift waves, respectively. Thus, Hall drift wave is associated with inhomogeneous plasmas since it depends on  $\nabla n$ . For instance, consider the inhomogeneous plasma density along x with an ambient magnetic field in the z-direction. The ambient magnetic field ( $\mathbf{B} = B_0 \hat{e}_z$ ) is then perturbed with  $\delta B_z \propto exp(ik_y y - i\omega t)$  giving rise to the following linear dispersion equation

$$\frac{\partial \delta \mathbf{B}}{\partial t} = \frac{1}{n_e^2 e} \nabla n \times (\delta \mathbf{J} \times \mathbf{B}) \tag{80}$$

Linearizing above gives

$$i\omega\delta B_z = \frac{1}{n_c^2 e} \frac{\partial n}{\partial x} \delta J_x B_z \tag{81}$$

Since  $\delta J_x = \frac{ik_y}{\mu_0} \delta B_z$  and  $n = n_e$  for Hydrogen plasma, the dispersion relation is then

$$\omega = \frac{k_y B_z}{n\mu_0} \frac{\partial n}{\partial x} = k_y V_A \frac{c}{L_n \omega_{vi}} \tag{82}$$

where  $L_n = (\frac{\partial \ln n}{\partial x})^{-1}$  is density gradient length scale,  $V_A = \frac{B_z}{\sqrt{\mu_0 m_i n}}$  is Alfven wave speed and  $\omega_{pi} = \sqrt{\frac{e^2 n}{\epsilon_0 m_i}}$  is the Hydrogen ion plasma frequency. Since Hall term is crucial for this problem,  $L_n < \frac{c}{\omega_{pi}}$  to generate Hall drift wave which propagates in the  $\mathbf{B} \times \nabla n$  direction. The problem is then set up on a computational domain of  $[-0.3, 0] \times [0.3, 0.2]$  where the number of grid points are (200, 120). Hydrogen plasma is used and has a number density profile of [34]

$$n(x) = \frac{n_0}{2} \left[ (1+A) + (1-A) \tanh\left(\frac{x-x_0}{\Delta x}\right) \right]$$
 (83)

where  $x_0=10$ cm,  $\Delta x=3$ cm and Atwood number is set as A=20 with a low number density of  $n_0=10^{18} {\rm m}^{-3}$  where Hall effect is significant. This means that the dimensional constants for the PDEs are also adjusted such that  $n_0=10^{18},\ L_0=1$  and  $B_0$  set to 0.4568 such that the dimensionless coefficient  $(\frac{B_0^2}{\mu_0 n_0 m_i v^2})$  for the explicit source terms is approximately 1. The density profile is then maintained by setting  $u_x=0$  every timestep. The plasma is also assumed to be isothermal  $(T\equiv {\rm const.})$  and for the ideal MHD components, HLLD Riemann solver [23] is used. Magnetic field is set along the z direction where  $B_0=0.1{\rm T}$  with perturbation of  $\delta B_z=\delta B\cos\left(\frac{2\pi my}{L_y}\right)$  in the y-direction where  $\delta B=0.001{\rm T}$  and m is

the mode number. The plasma beta  $(\beta)$  is then set to 0.0001 at peak density region where x=0. This allows the Hall drift wave to propagate in the y-direction.

For this problem, the maximum phase velocity of the Hall drift wave is expected to occur at  $x \simeq 15$ cm. From Fig. 9a, the magnetic field  $(B_z)$  contours are distorted in the y-direction in the density gradient region and the maximum distortion occurs at around 15cm along x-axis. Some discrepancy is expected since electron inertia effects and Ohmic resistivity are not set to zero  $(\eta = 10^{-8})$  here. For instance, from Fig. 9a, there appear to be some  $B_z$  diffusion at |x| > 0.2.

# 4.5. 2D MHD blast wave problem

This is done on a computational domain of  $[-0.5, 0.5] \times [-0.75, 0.75]$  with grid resolution of 200 by 300. The background pressure is set to  $0.1\rho_0$  while the center spherical region of radius 0.1 has a pressure of  $10\rho_0$ . The density of the gas is  $\rho_0$  while the velocities are 0 everywhere. Uniform magnetic field along y and z components are applied and they have values of  $\sqrt{0.5\rho_0}$  and  $\sqrt{0.5\rho_0}$ , respectively. The heat capacity ratio is set to  $\frac{5}{3}$  here. For the ideal MHD case,  $\rho_0$  is 1 and to test for the increment of non-ideal effects,  $\rho_0$  is decreased to 0.1. This can be seen from Figs. 10 and 11 where the increment of non-ideal effects causes the ratio of the out-of-plane z-components for both velocity and magnetic field to the in-plane components to increase.

## 4.6. 2D MHD rotor problem

Rotor problem is also included to study the onset and propagation of strong torsional Alfven waves in both ideal and non-ideal regimes. Parthenon's in-built adaptive mesh refinement (AMR), featuring a uniquely designed second-order prolongation and restriction scheme that preserves  $\nabla \cdot \mathbf{B} \approx 0$  [36], is also tested with the XMHD solver. This is done using a computational domain of  $[-0.5, 0.5] \times [-0.5, 0.5]$  with base grid resolution of 100 by 100 and 3 levels of adaptive grid refinement. The heat capacity ratio is set to 1.4 here. For the ideal MHD case,  $\rho_0$  is 1 and to test for the increment of non-ideal effects,  $\rho_0$  is decreased to 0.1.

$$\rho(x,y) = \begin{cases}
10, & r \le r_0, \\
1 + 9 f(r), & r_0 < r < r_1, & p(x,y) = 1 \\
1, & r \ge r_1
\end{cases}$$

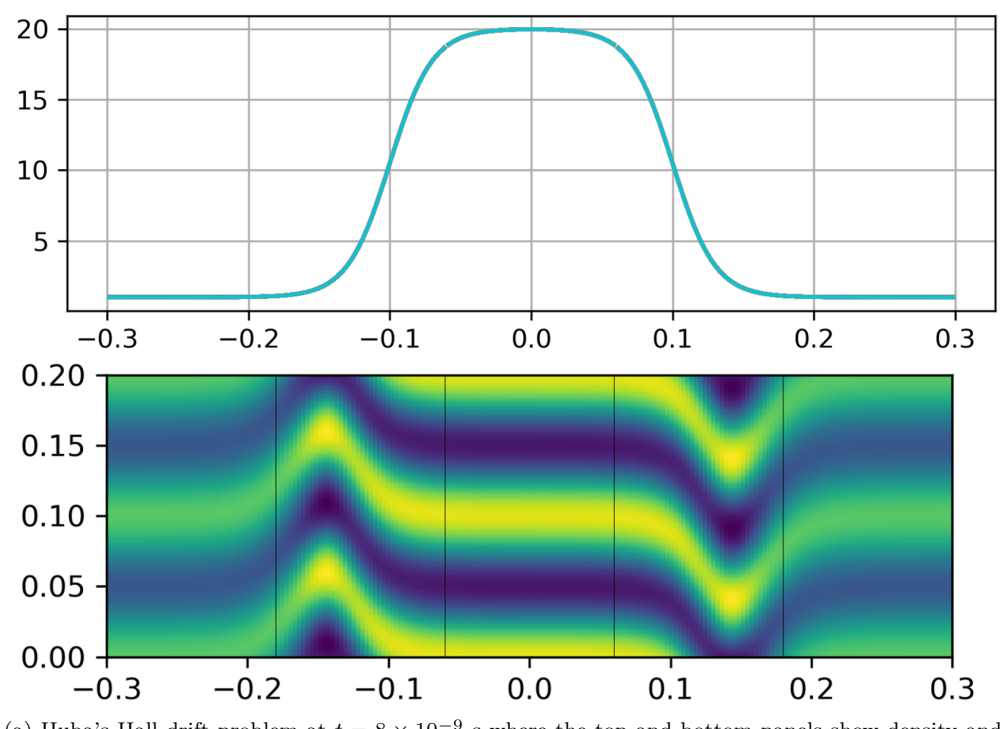
$$u(x,y) = \begin{cases}
-u_0 y, & r \le r_0, \\
-f(r) u_0 y, & r_0 < r < r_1, & v(x,y) = \begin{cases}
u_0 x, & r \le r_0, \\
f(r) u_0 x, & r_0 < r < r_1, \\
0, & r \ge r_1
\end{cases}$$
(84)

$$u(x,y) = \begin{cases} -u_0 y, & r \le r_0, \\ -f(r) u_0 y, & r_0 < r < r_1, \\ 0, & r \ge r_1 \end{cases} \qquad v(x,y) = \begin{cases} u_0 x, & r \le r_0, \\ f(r) u_0 x, & r_0 < r < r_1, \\ 0, & r \ge r_1 \end{cases}$$
(85)

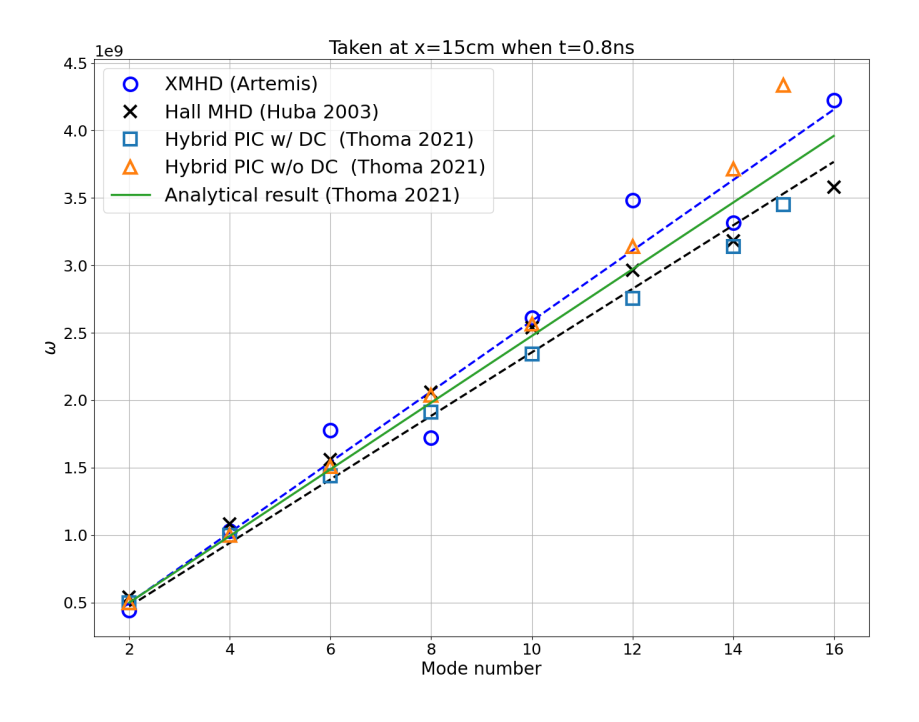
$$B_x(x,y) = \frac{5}{\sqrt{4\pi}}$$
  $B_y(x,y) = 0$  (86)

where

$$u_0 = 20,$$
  $r_0 = 0.1,$   $r_1 = 0.115,$   $r = \sqrt{x^2 + y^2},$   $w = B_z = 0,$ 



(a) Huba's Hall drift problem at  $t=8\times 10^{-9}$  s where the top and bottom panels show density and magnetic field  $B_z(x,y)$ , respectively. Note that both are normalized by  $n_0$  and  $B_0$  here.



(b) Dashed line based on the linear fit of XMHD (Artemis) and Hall MHD [34] are added to show linear dispersion relation obtained from the Hall drift problem. Results from Hybrid PIC [35] with or without displacement current (DC) are also included for comparison.

Figure 9: Results for Huba's Hall drift problem obtained from XMHD implemented on Artemis and compared to Hall MHD and Hybrid PIC results.

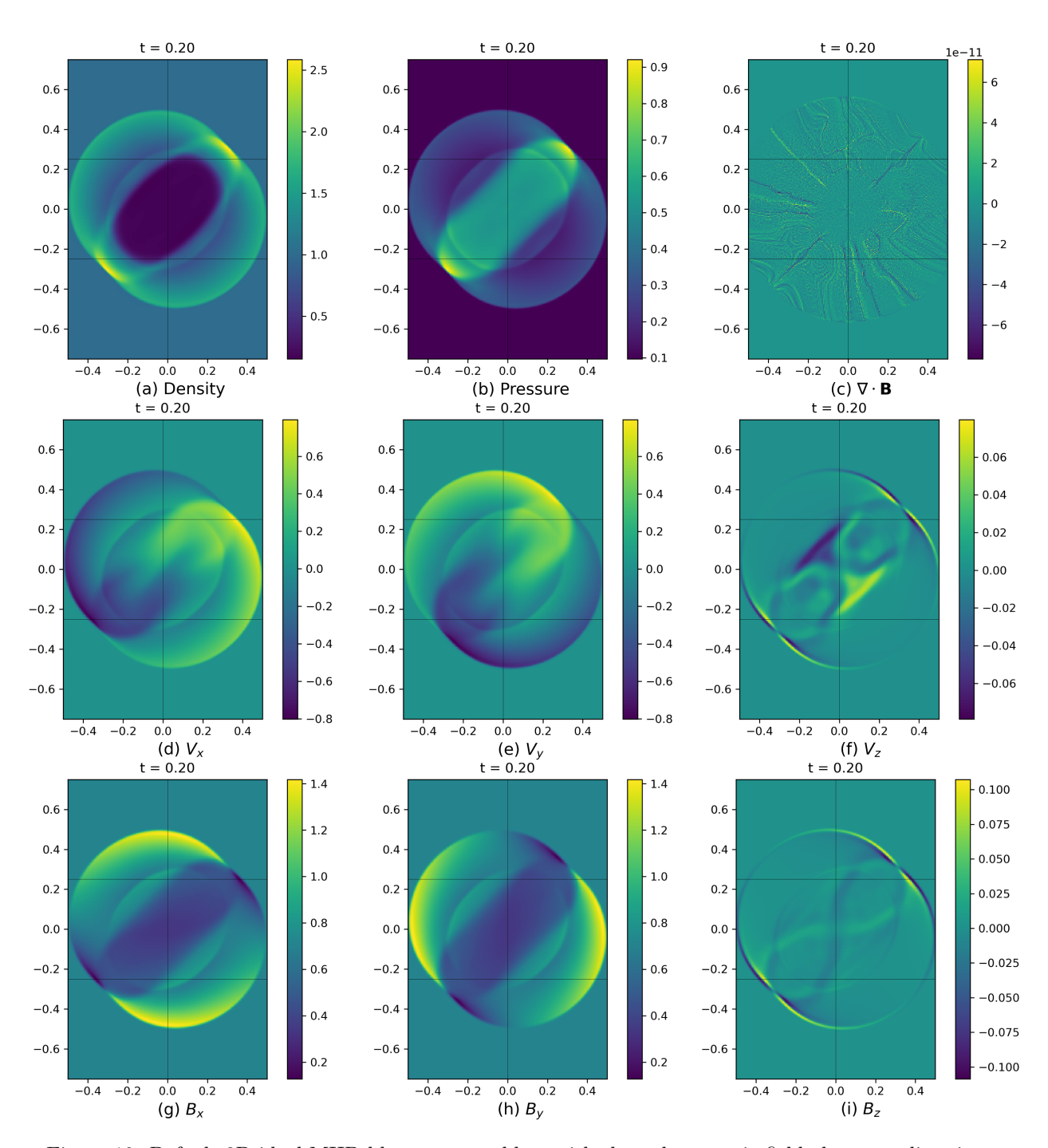


Figure 10: Default 2D ideal MHD blast wave problem with slanted magnetic field along x-y direction.

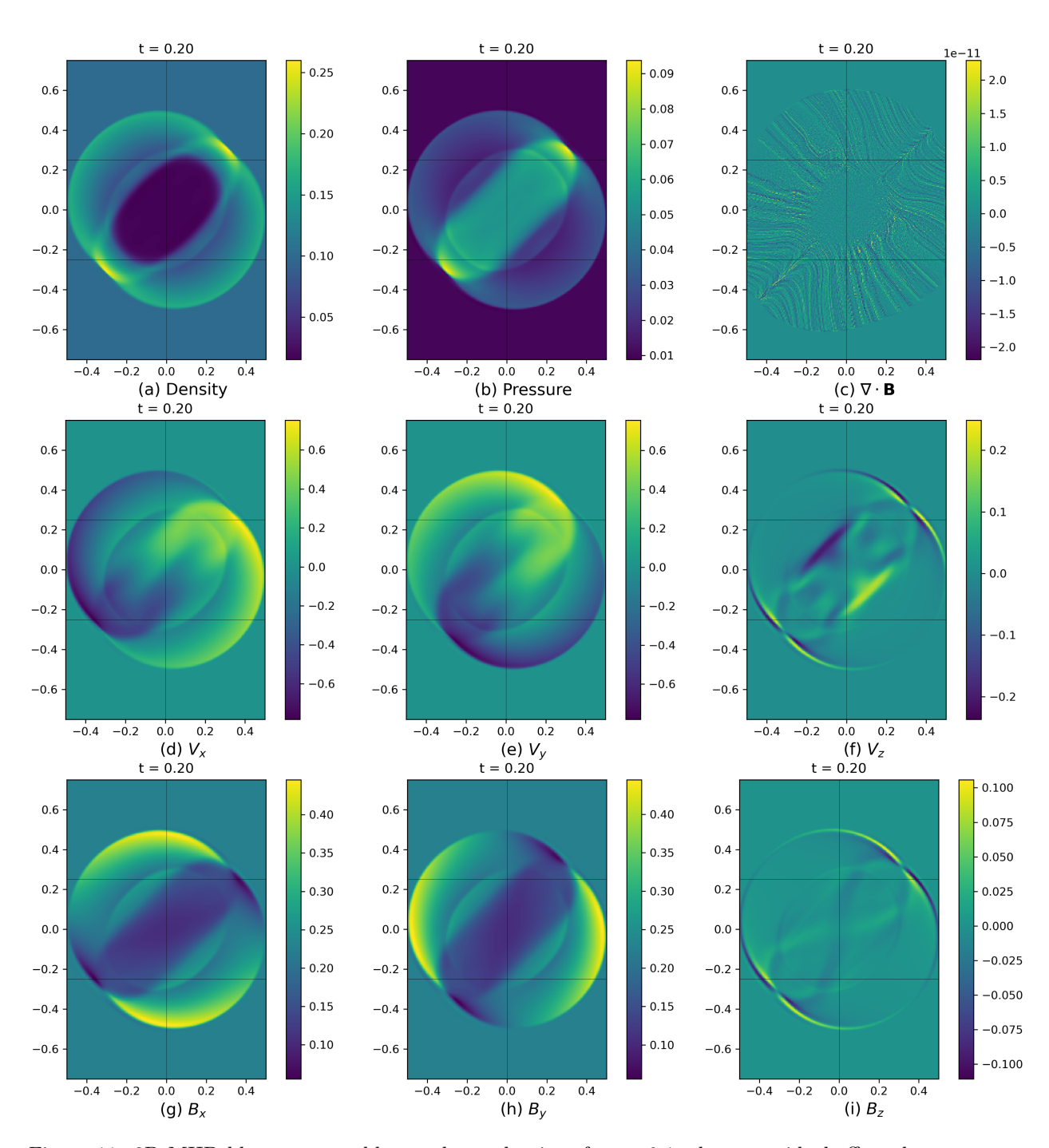


Figure 11: 2D MHD blast wave problem at lower density of  $\rho_0 = 0.1$  where non-ideal effects become more significant.

and the linear taper function which may be used to prevent strong transients start-up during computation [21],

$$f(r) = \frac{r_1 - r}{r_1 - r_0}.$$

Since the pressure is uniform initially unlike density, density gradient is used as the criteria for AMR here. Similar to the blast wave problem, decreasing density causes the out-of-plane z-components for both velocity and magnetic field to the in-plane components to increase as shown in Figs. 12 and 13.

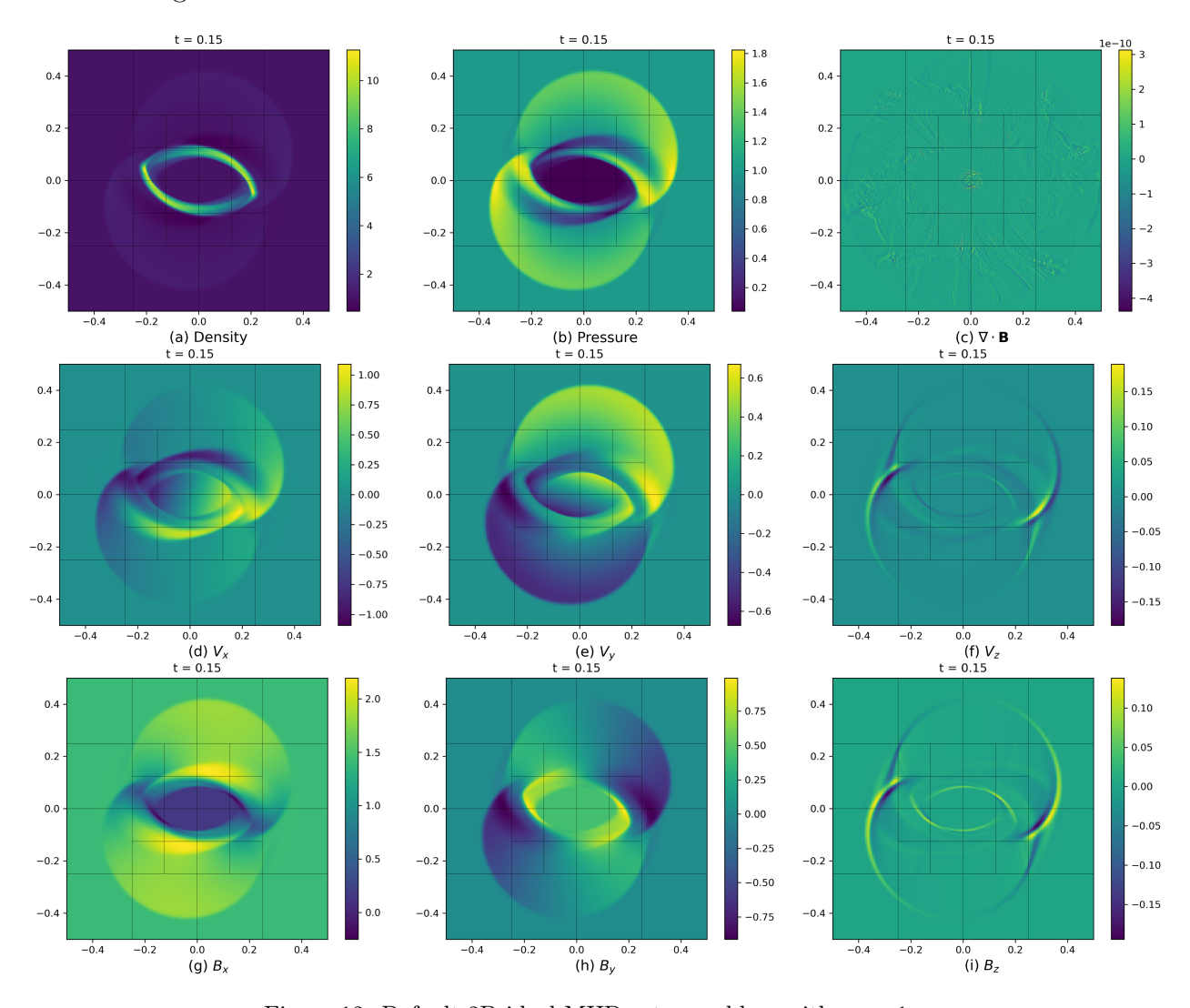


Figure 12: Default 2D ideal MHD rotor problem with  $\rho_0 = 1$ .

## 5. Conclusion

The development of a semi-implicit finite-volume schemes for solving the XMHD equations while retaining most of the already well-established ideal MHD framework has been the sub-

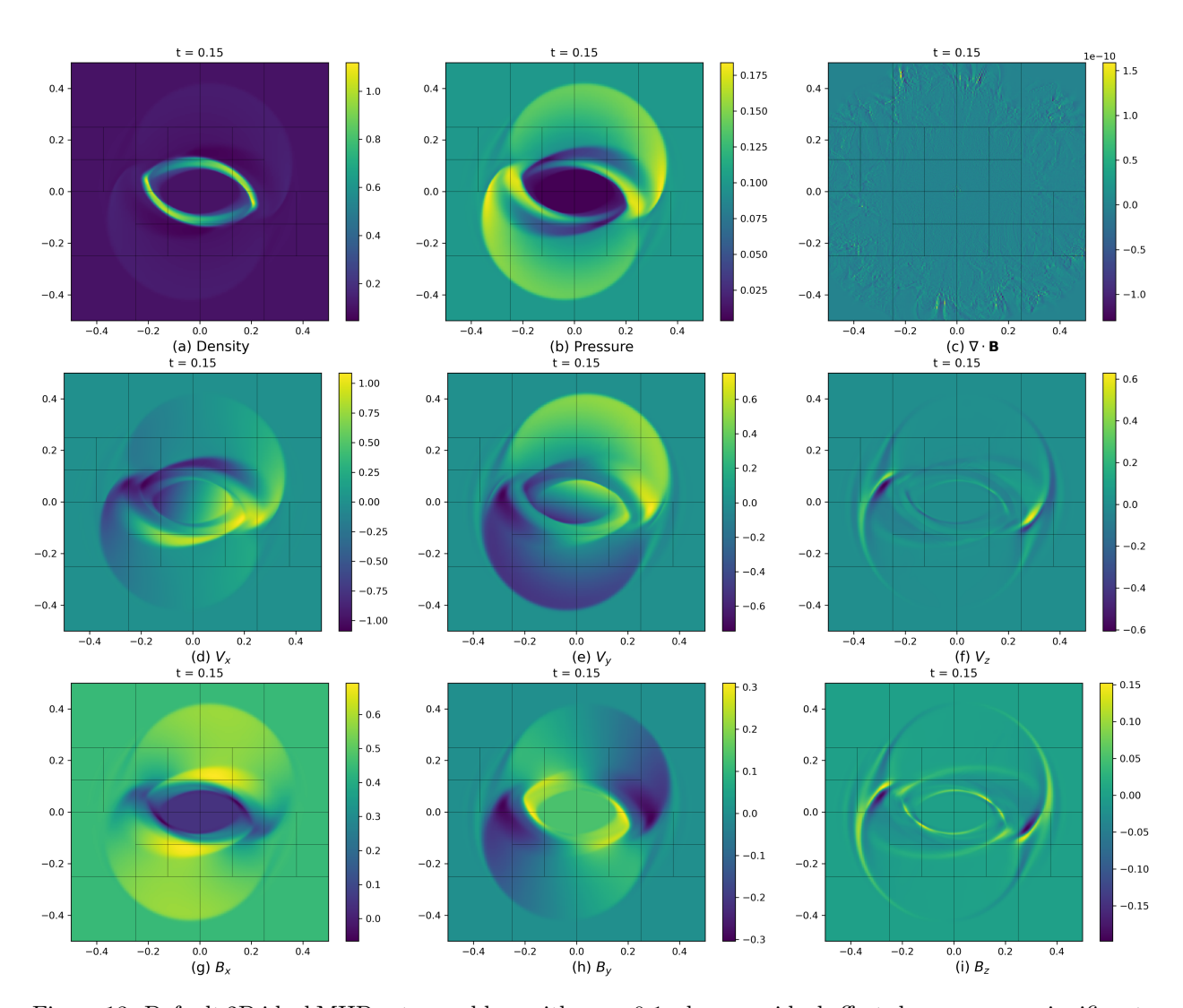


Figure 13: Default 2D ideal MHD rotor problem with  $\rho_0=0.1$  when non-ideal effects become more significant.

ject of the work. The goal is to ensure that the XMHD solver is asymptotically preserving in terms of producing similar results to existing ideal MHD solver. Additionally, the XMHD solver developed here has shown promising results at the resistive and Hall limits. This potentially enables the current solver to handle a wider range of density regimes, which is particularly important for high-energy-density (HED) plasma systems. Such systems often exhibit large density variations that must be accurately captured to improve one's understanding and control of the plasma's energy and stability.

This is accomplished by first re-writing the governing equations such that it preserves most of the ideal MHD framework, allowing existing ideal MHD solvers or algorithms to be reused. For instance, the advantage of preserving locally divergence-free magnetic field by placing magnetic-field at face-center through constrained transport method is employed in this XMHD solver. Naturally, the E field is placed at cell edges, together with J field for consistency during implicit source terms update. However, the implicit source term update requires directional splitting to avoid spatial biasing since it requires all of the edge-centered J and E components which are not co-located. The Jacobian matrix for the governing equations without the source terms is also obtained to determine the diffusive stabilization for the non-ideal components of the LLF Riemann solver evaluated at the cell faces. But this is not sufficient stability-wise, especially at low density where non-ideal effects become significant and therefore, a density-dependent slope limiter is used to increase flux diffusivity away from the continuum limit. Finally, since all the variables are not co-located, interpolation of values across different topological elements of the computational cell is required and simple arithmetic averaging seems sufficient for the test problems here.

There are other aspects of the current algorithm that require further understanding and improvement. For example, the solver includes two stiff terms (i.e.,  $\epsilon_E$  and  $\epsilon_J$ ) that depend on the dimensional constants used to non-dimensionalize the XMHD equations. At present, these constants are chosen such that  $\frac{B_0^2}{\mu_0 n_0 m_i v^2} \approx 1$ , as this choice simplifies the problem; however, it has been shown that this does not necessarily yield the most accurate results. Instead, the ratio of the timestep dt to  $\epsilon_E$  and  $\epsilon_J$  may influence how effectively the system relaxes towards the appropriate physical limit. Future work will involve additional tests and analysis to better understand this relationship. Furthermore, there are several potential avenues for enhancing the current algorithm such as

- Directionally unsplit the implicit source term update for improved stability.
- IMEX or linear analysis can be used to increase the order of accuracy for the implicit source term update, which is currently at most 1st-order.
- Upwind constrained transport method can be used instead. Additionally, the concept of upwind constrained transport method can be applied to the non-ideal source term used to update the magnetic field, although the **E** field must be accounted for during the upwinding.
- Adding ambipolar diffusion to the right-hand side of GOL and testing it against field diffusion with an initial Gaussian profile because it has an analytical solution.

# Acknowledgement

This work was funded by Los Alamos National Laboratory under the grant "Algorithm/hardware/software Co-design for High Energy Density Applications," at the University of Michigan. The authors are grateful to Jonah Miller and Patrick Mullen for valuable advise on this work.

# Appendix A. Re-writing XMHD equations

The derivation of Eqs. 8 - 14 from Eqs. 1 - 7 requires the following vector and vector calculus identities,

$$\nabla \cdot (\mathbf{A}\mathbf{B}) = \mathbf{B}(\nabla \cdot \mathbf{A}) + (\mathbf{A} \cdot \nabla)\mathbf{B} \tag{A.1}$$

$$\nabla \times (\mathbf{A} \times \mathbf{B}) = \nabla \cdot (\mathbf{B}\mathbf{A} - \mathbf{A}\mathbf{B}) \tag{A.2}$$

$$\nabla(\mathbf{A} \cdot \mathbf{B}) = (\mathbf{A} \cdot \nabla)\mathbf{B} + \mathbf{A} \times (\nabla \times \mathbf{B}) + (\mathbf{B} \cdot \nabla)\mathbf{A} + \mathbf{B} \times (\nabla \times \mathbf{A})$$
(A.3)

$$\nabla \cdot (\mathbf{A} \times \mathbf{B}) = (\nabla \times \mathbf{A}) \cdot \mathbf{B} - (\nabla \times \mathbf{B}) \cdot \mathbf{A} \tag{A.4}$$

$$\mathbf{A} \cdot (\mathbf{B} \times \mathbf{C}) = (\mathbf{A} \times \mathbf{B}) \cdot \mathbf{C} = -\mathbf{A} \cdot (\mathbf{C} \times \mathbf{B}) \tag{A.5}$$

$$\mathbf{A} \times (\mathbf{B} \times \mathbf{C}) = (\mathbf{A} \cdot \mathbf{C})\mathbf{B} - (\mathbf{A} \cdot \mathbf{B})\mathbf{C}$$
(A.6)

where  $AB \equiv A \otimes B$ .

From Eq. 2,

$$\begin{split} \frac{\partial}{\partial t}(\rho \mathbf{u}) + \nabla \cdot (\rho \mathbf{u} \mathbf{u} + P \mathbb{I}) &= \mathbf{J} \times \mathbf{B} \\ &= \frac{1}{\mu_0} \left( \nabla \times \mathbf{B} \right) \times \mathbf{B} + \left( \mathbf{J} - \frac{1}{\mu_0} \nabla \times \mathbf{B} \right) \times \mathbf{B} \\ &= \frac{1}{\mu_0} \left[ (\mathbf{B} \cdot \nabla) \mathbf{B} - \frac{1}{2} \nabla (\mathbf{B} \cdot \mathbf{B}) \right] + \left( \mathbf{J} - \frac{1}{\mu_0} \nabla \times \mathbf{B} \right) \times \mathbf{B} \\ &= \frac{1}{\mu_0} \left[ \nabla \cdot (\mathbf{B} \mathbf{B}) - \frac{1}{2} \nabla \cdot (B^2 \mathbb{I}) \right] + \left( \mathbf{J} - \frac{1}{\mu_0} \nabla \times \mathbf{B} \right) \times \mathbf{B} \end{split}$$

where bringing over the divergence term on the right-hand side to the left side of the equation recovers Eq. 9.

As for Eq. 4,

$$\begin{split} \frac{\partial \mathbf{B}}{\partial t} &= -\nabla \times \mathbf{E} \\ &= \nabla \times (\mathbf{u} \times \mathbf{B}) - \nabla \times (\mathbf{E} + \mathbf{u} \times \mathbf{B}) \\ &= \nabla \cdot (\mathbf{B} \mathbf{u} - \mathbf{u} \mathbf{B}) - \nabla \times (\mathbf{E} + \mathbf{u} \times \mathbf{B}) \end{split}$$

Similarly, the divergence on the right-hand side of the equation is carried to the left to give Eq. 11.

Finally for energy equation from Eq. 3,

$$\frac{\partial E_n}{\partial t} + \nabla \cdot [\mathbf{u}(E_n + P)] = \mathbf{u} \cdot (\mathbf{J} \times \mathbf{B}) + \eta J^2$$

$$= \mathbf{u} \cdot \left[ \frac{1}{\mu_0} (\nabla \times \mathbf{B}) \times \mathbf{B} \right] + \mathbf{u} \cdot \left[ \left( \mathbf{J} - \frac{1}{\mu_0} \nabla \times \mathbf{B} \right) \times \mathbf{B} \right] + \eta J^2$$
(A.7)

To further expand the right-hand side of Eq. A.7, take the dot product of Eq. 11 with  $\frac{1}{\mu_0}$ **B** as follows,

$$\frac{\partial}{\partial t} \left( \frac{1}{2\mu_0} B^2 \right) = \frac{1}{\mu_0} \mathbf{B} \cdot [\nabla \times (\mathbf{u} \times \mathbf{B})] - \frac{1}{\mu_0} \mathbf{B} \cdot [\nabla \times (\mathbf{E} + \mathbf{u} \times \mathbf{B})]$$

$$= \frac{1}{\mu_0} [\nabla \cdot [(\mathbf{u} \times \mathbf{B}) \times \mathbf{B}] + (\mathbf{u} \times \mathbf{B}) \cdot (\nabla \times \mathbf{B})] - \frac{1}{\mu_0} \mathbf{B} \cdot [\nabla \times (\mathbf{E} + \mathbf{u} \times \mathbf{B})]$$

$$= \frac{1}{\mu_0} [\nabla \cdot [(\mathbf{u} \times \mathbf{B}) \times \mathbf{B}] + \mathbf{u} \cdot (\mathbf{B} \times (\nabla \times \mathbf{B})] - \frac{1}{\mu_0} \mathbf{B} \cdot [\nabla \times (\mathbf{E} + \mathbf{u} \times \mathbf{B})]$$
(A.8)

This gives

$$\mathbf{u} \cdot \left[ \frac{1}{\mu_0} (\nabla \times \mathbf{B}) \times \mathbf{B} \right] = -\frac{\partial}{\partial t} \left( \frac{1}{2\mu_0} B^2 \right) + \frac{1}{\mu_0} \nabla \cdot \left[ (\mathbf{u} \times \mathbf{B}) \times \mathbf{B} \right] - \frac{1}{\mu_0} \mathbf{B} \cdot \left[ \nabla \times (\mathbf{E} + \mathbf{u} \times \mathbf{B}) \right]$$
(A.9)

which can be substituted into the right-hand side of Eq. A.7,

$$\frac{\partial E_n}{\partial t} + \nabla \cdot [\mathbf{u}(E_n + P)] = -\frac{\partial}{\partial t} \left( \frac{1}{2\mu_0} B^2 \right) + \frac{1}{\mu_0} \nabla \cdot [(\mathbf{u} \times \mathbf{B}) \times \mathbf{B}] - \frac{1}{\mu_0} \mathbf{B} \cdot [\nabla \times (\mathbf{E} + \mathbf{u} \times \mathbf{B})] + \mathbf{u} \cdot \left[ \left( \mathbf{J} - \frac{1}{\mu_0} \nabla \times \mathbf{B} \right) \times \mathbf{B} \right] + \eta J^2$$
(A.10)

Bringing over the first two right-hand terms of above Eq. A.10 to the left will recover Eq. 10.

## Appendix B. Deriving dimensionless XMHD equations

To non-dimensionalized XMHD equations from Eqs. 8 - 14 to Eqs. 15 -21, the following conversions must be used.

$$P_{0} = n_{0}m_{i}v^{2}, \quad E_{0} = vB_{0}, \quad J_{0} = \frac{B_{0}}{\mu_{0}L_{0}}, \quad v_{A} = \frac{B_{0}}{\sqrt{n_{0}m_{i}\mu_{0}}}, \quad v = \frac{L_{0}}{t_{0}}$$

$$x = L_{0}x^{*}, \quad t = t_{0}t^{*}, \quad n_{e} = Zn_{0}\rho^{*}, \quad P = P_{0}P^{*}, \quad P_{e} = P_{0}P^{*}_{e},$$

$$\mathbf{u} = v\mathbf{u}^{*}, \quad \mathbf{B} = B_{0}\mathbf{B}^{*}, \quad \mathbf{E} = E_{0}\mathbf{E}^{*}, \quad \mathbf{J} = J_{0}\mathbf{J}^{*}$$
(B.1)

where  $\epsilon_0 \approx 8.854 \times 10^{-12}$ ,  $\mu_0 = 4\pi \times 10^{-7}$  and  $(\cdot)^*$  denotes dimensionless variables. Note that  $L_0$  and  $t_0$  are chosen such that  $v = v_A$  which allows the dimensional coefficients to be largely canceled out.

# Appendix C. Temperature relaxation

As mentioned in Sect. 2.2, the electron-ion energy exchange source term is demonstrated here and this starts by non-dimensionalizing Eq. 26 to get

$$\frac{\partial \tilde{S}_e}{\partial \tilde{t}} + \tilde{\nabla} \cdot (\tilde{\mathbf{u}}_e \tilde{S}_e) = \tilde{n}_e^{1-\gamma} (\gamma - 1) \left[ \frac{k_B T_0}{m_i v^2} \frac{m_e}{m_i + m_e} \frac{\tilde{n}_e}{\tilde{\tau}_{ei}} (\tilde{T}_i - \tilde{T}_e) + \xi_{ei} \tilde{\eta} \tilde{J}^2 \right]$$
(C.1)

where tilde variables denote dimensionless variables. Note that  $k_B T_0 = m_i v^2$  since  $T_0$  is derived from  $P_0 = n_0 m_i v^2$  and ideal gas is assumed here.  $\zeta_{ei}$  will be taken as 1 for simplicity by assuming that Ohmic heating between electrons and ions are similar. If  $\tilde{\tau}_{ei}$  is very small, implicit solve is required but for the problem here, this term is not stiff and thus, explicit update is used instead.

FLASH model [37] can then be used for the electron-ion relaxation time as follows,

$$\tau_{ei} = \frac{3k_B^{3/2}}{8\sqrt{2\pi}e^4} \frac{(m_i T_e + m_e T_i)^{3/2}}{(m_e m_i)^{1/2} Z^2 n_i \ln \Lambda}$$
(C.2)

where Coulomb logarithm is taken as 5. Substituting into Eq. C.1 and re-writing it to show the explicit dependence on  $n_e = n_0 \tilde{n}_e$  for the electron-ion temperature difference

$$\frac{\partial \tilde{S}_e}{\partial \tilde{t}} + \tilde{\nabla} \cdot (\tilde{\mathbf{u}}_e \tilde{S}_e) = \tilde{n}_e^{1-\gamma} (\gamma - 1) \left[ \frac{m_e}{m_i + m_e} t_0 \frac{8\sqrt{2\pi}e^4}{3k_B^{3/2}} \frac{(m_e m_i)^{1/2} Z n_0 \ln \Lambda}{T_0^{3/2} m_e^{3/2}} \tilde{n}_e \frac{(\tilde{T}_i^* - \tilde{T}_e^*)}{(\frac{m_e}{m_e} \tilde{T}_e^* + \tilde{T}_i^*)^{3/2}} + \tilde{\eta} \tilde{J}^2 \right]$$
(C.3)

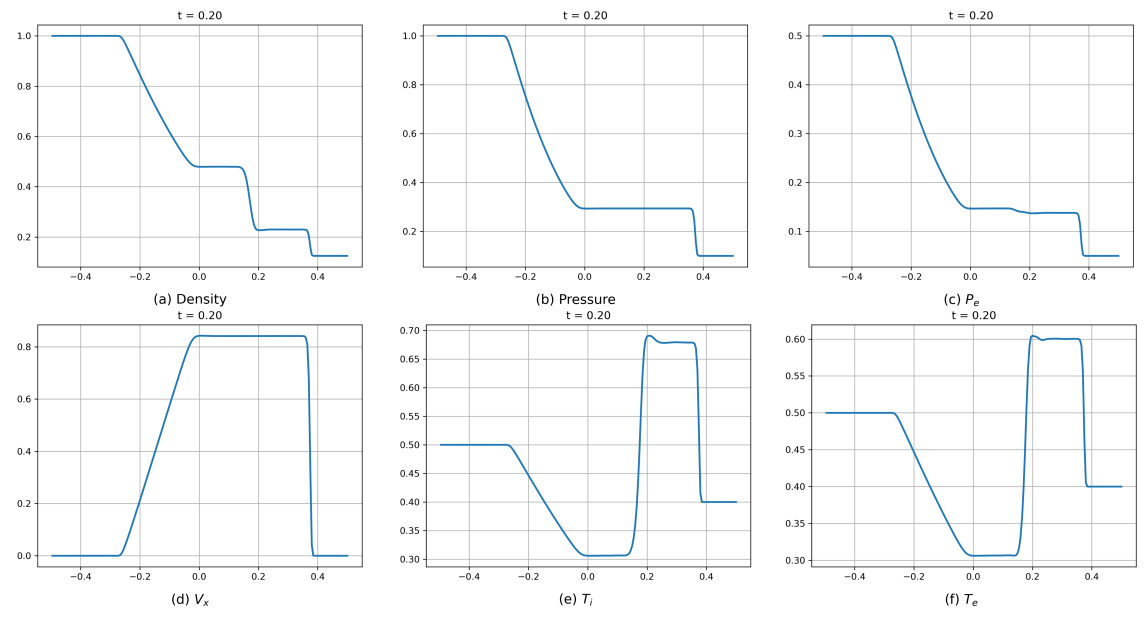
To test whether the electron-ion energy exchange source term is working in terms of equilibrating electron and ion temperatures, Sod shock tube (e.g., plasma  $\beta \to \infty$  thus  $B_0 = 0$ ) for Hydogen plasma is considered as follows,

$$(\rho, u_x, u_y, u_z, P, P_e, B_x, B_y, B_z) = \begin{cases} (1.000, 0, 0, 0, 1.0, 0.50, 0, 0, 0), & \text{if } x \le 0 \\ (0.125, 0, 0, 0, 0.1, 0.05, 0, 0, 0), & \text{if } x > 0 \end{cases}$$

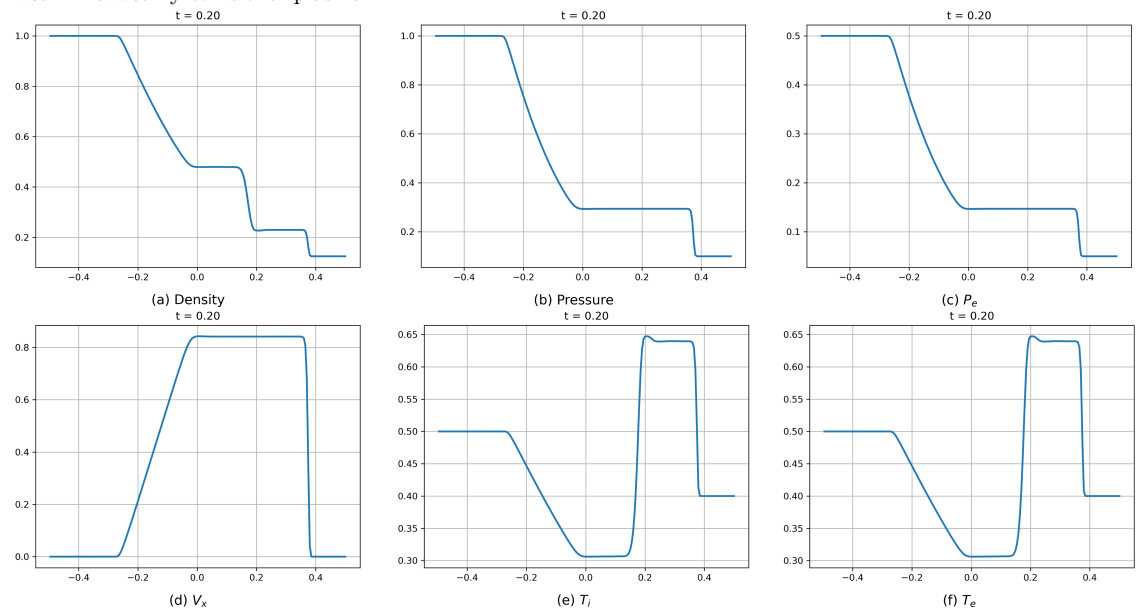
where  $L_0 = 10^4$  and  $t_0 = 10^2$  are chosen such that the electron-ion energy exchange source term becomes significant. Two densities,  $n_0 = 10^{20} \,\mathrm{m}^{-3}$  and  $n_0 = 10^{30} \,\mathrm{m}^{-3}$ , are used to test weakly and strongly collisional regimes, respectively, with the latter expected to yield  $T_e = T_i$ . The results in Fig. C.14 show that only the dense plasma reaches ion–electron temperature equilibrium by the end of the simulation.

# References

[1] C. A. Walsh, J. P. Chittenden, D. W. Hill, and C. Ridgers, "Extended-magnetohydrodynamics in under-dense plasmas," *Physics of Plasmas*, vol. 27, p. 022103, 02 2020.



(a) For  $n_0 = 10^{20} \mathrm{m}^{-3}$ , the post-shock electron temperature is expected to be lower than the ion temperature, since electrons experience primarily adiabatic compression heating, whereas electron–ion energy exchange remains weak in a weakly collisional plasma.



(b) At  $n_0 = 10^{30} \mathrm{m}^{-3}$  where both ions and electrons temperatures are expected to equilibrate at end time.

Figure C.14: Sod shock tube problem is used to test for the electron-ion energy exchange source term at different densities.

- [2] J. M. Woolstrum, D. A. Yager-Elorriaga, P. C. Campbell, N. M. Jordan, C. E. Seyler, and R. D. McBride, "Extended magnetohydrodynamics simulations of thin-foil z-pinch implosions with comparison to experiments," *Physics of Plasmas*, vol. 27, p. 092705, 09 2020.
- [3] J. R. Young, M. B. Adams, H. Hasson, I. West-Abdallah, M. Evans, and P.-A. Gourdain, "Using extended mhd to explore lasers as a trigger for x-pinches," *Physics of Plasmas*, vol. 28, p. 102703, 10 2021.
- [4] A. Kleiner, N. M. Ferraro, R. Sweeney, B. C. Lyons, and M. Reinke, "Extended-MHD simulations of disruption mitigation via massive gas injection in SPARC," *Nuclear Fusion*, vol. 65, no. 2, p. 026015, 2025. Published 30 December 2024. © 2024 The Author(s). Open access.
- [5] N. D. Hamlin and C. E. Seyler, "Power flow in pulsed-power systems: The influence of hall physics and modeling of the plasma-vacuum interface," *IEEE Transactions on Plasma Science*, vol. 47, no. 5, pp. 2064–2073, 2019.
- [6] R. D. Hazeltine, *The Framework of Plasma Physics*. Boca Raton: CRC Press, 1st ed., 2004. eBook published March 7, 2018.
- [7] N. Krall and A. Trivelpiece, *Principles of Plasma Physics*. International series in pure and applied physics, McGraw-Hill, 1973.
- [8] L. Spitzer, Physics of Fully Ionized Gases. 1956.
- [9] L. Chacón and D. Knoll, "A 2d high- $\beta$  hall mhd implicit nonlinear solver," *Journal of Computational Physics*, vol. 188, no. 2, pp. 573–592, 2003.
- [10] A. Hakim, J. Loverich, and U. Shumlak, "A high resolution wave propagation scheme for ideal two-fluid plasma equations," *Journal of Computational Physics*, vol. 219, no. 1, pp. 418–442, 2006.
- [11] A. H. Hakim, "Extended mhd modelling with the ten-moment equations," *Journal of Fusion Energy*, vol. 27, no. 1, pp. 36–43, 2008.
- [12] J. D. Huba, "Numerical methods: Ideal and hall mhd," in *Proceedings of ISSS*, vol. 7, pp. 26–31, March 2005.
- [13] J. Loverich and U. Shumlak, "A discontinuous galerkin method for the full two-fluid plasma model," *Computer Physics Communications*, vol. 169, no. 1, pp. 251–255, 2005. Proceedings of the Europhysics Conference on Computational Physics 2004.
- [14] U. Shumlak and J. Loverich, "Approximate riemann solver for the two-fluid plasma model," *Journal of Computational Physics*, vol. 187, no. 2, pp. 620–638, 2003.

- [15] J. D. Huba and J. G. Lyon, "A new 3d mhd algorithm: the distribution function method," *Journal of Plasma Physics*, vol. 61, no. 3, pp. 391–405, 1999. Received 20 May 1998; revised 17 November 1998.
- [16] X. Zhao, Y. Yang, and C. E. Seyler, "A positivity-preserving semi-implicit discontinuous galerkin scheme for solving extended magnetohydrodynamics equations," *Journal of Computational Physics*, vol. 278, pp. 400–415, 2014.
- [17] C. E. Seyler and M. R. Martin, "Relaxation model for extended magnetohydrodynamics: Comparison to magnetohydrodynamics for dense z-pinches," *Physics of Plasmas*, vol. 18, p. 012703, 01 2011.
- [18] A. Sangam, Élise Estibals, and H. Guillard, "Derivation and numerical approximation of two-temperature euler plasma model," *Journal of Computational Physics*, vol. 444, p. 110565, 2021.
- [19] P. Grete, J. C. Dolence, J. M. Miller, J. Brown, B. Ryan, A. Gaspar, F. Glines, S. Swaminarayan, J. Lippuner, C. J. Solomon, G. Shipman, C. Junghans, D. Holladay, J. M. Stone, and L. F. Roberts, "Parthenon—a performance portable block-structured adaptive mesh refinement framework," *International Journal of High Performance Computing Applications*, vol. 37, 12 2022.
- [20] J. M. Stone, K. Tomida, C. J. White, and K. G. Felker, "The athena++ adaptive mesh refinement framework: Design and magnetohydrodynamic solvers," *The Astrophysical Journal Supplement Series*, vol. 249, p. 4, July 2020.
- [21] D. S. Balsara and D. S. Spicer, "A staggered mesh algorithm using high order godunov fluxes to ensure solenoidal magnetic fields in magnetohydrodynamic simulations," *Journal of Computational Physics*, vol. 149, no. 2, pp. 270–292, 1999.
- [22] P. D. Lax, "Weak solutions of nonlinear hyperbolic equations and their numerical computation," Communications on Pure and Applied Mathematics, vol. 7, no. 1, pp. 159–193, 1954.
- [23] T. Miyoshi and K. Kusano, "A multi-state HLL approximate Riemann solver for ideal magnetohydrodynamics," *Journal of Computational Physics*, vol. 208, pp. 315–344, Sept. 2005.
- [24] L. N. Trefethen and D. Bau, Numerical Linear Algebra, Twenty-fifth Anniversary Edition. Philadelphia, PA: Society for Industrial and Applied Mathematics, 2022.
- [25] C.-W. Shu and S. Osher, "Efficient implementation of essentially non-oscillatory shock-capturing schemes," *Journal of Computational Physics*, vol. 77, no. 2, pp. 439–471, 1988.

- [26] B. Van Leer, "Towards the ultimate conservative difference scheme iii. upstream-centered finite-difference schemes for ideal compressible flow," *Journal of Computational Physics*, vol. 23, no. 3, pp. 263–275, 1977.
- [27] R. E. Caflisch, S. Jin, and G. Russo, "Uniformly accurate schemes for hyperbolic systems with relaxation," *SIAM Journal on Numerical Analysis*, vol. 34, no. 1, pp. 246–281, 1997.
- [28] M. Brio and C. Wu, "An upwind differencing scheme for the equations of ideal magnetohydrodynamics," *Journal of Computational Physics*, vol. 75, no. 2, pp. 400–422, 1988.
- [29] J. M. Stone, T. A. Gardiner, P. Teuben, J. F. Hawley, and J. B. Simon, "Athena: A new code for astrophysical mhd," *The Astrophysical Journal Supplement Series*, vol. 178, pp. 137–177, Sept. 2008.
- [30] N. M. Ferraro, S. C. Jardin, and P. B. Snyder, "Ideal and resistive edge stability calculations with m3d-c1," *Physics of Plasmas*, vol. 17, p. 102508, 10 2010.
- [31] T. A. Gardiner and J. M. Stone, "An unsplit godunov method for ideal mhd via constrained transport in three dimensions," *Journal of Computational Physics*, vol. 227, no. 8, pp. 4123–4141, 2008.
- [32] K. Iwasaki and K. Tomida, "Comparative analysis of hall effect implementations in hall magnetohydrodynamics," *The Astrophysical Journal*, vol. 984, p. 50, apr 2025.
- [33] P. D. Mullen, Magnetized models for the formation of the Moon. PhD thesis, University of Illinois at Urbana-Champaign, Urbana, IL, August 2021. Ph.D. Dissertation.
- [34] J. D. Huba, *Hall Magnetohydrodynamics A Tutorial*, pp. 166–192. Berlin, Heidelberg: Springer Berlin Heidelberg, 2003.
- [35] C. Thoma, D. Welch, and D. Rose, "Implicit highly-coupled single-ion hall-mhd formulation for hybrid particle-in-cell codes," *Computer Physics Communications*, vol. 261, p. 107823, 2021.
- [36] G. Tóth and P. L. Roe, "Divergence- and Curl-Preserving Prolongation and Restriction Formulas," *Journal of Computational Physics*, vol. 180, pp. 736–750, Aug. 2002.
- [37] FLASH Center for Computational Science, University of Rochester, FLASH User's Guide (Development Version). University of Rochester, 2024. Development release, updated daily.